

ENVIRONMENTAL RESEARCH
LETTERS

LETTER

Global, regional and national trends of atmospheric ammonia derived from a decadal (2008–2018) satellite record

OPEN ACCESS

RECEIVED

17 November 2020

REVISED

14 December 2020

ACCEPTED FOR PUBLICATION

22 December 2020











PUBLISHED

6 May 2021

Original Content from this work may be used under the terms of the [Creative Commons Attribution 4.0 licence](https://creativecommons.org/licenses/by/4.0/).

Any further distribution of this work must maintain attribution to the author(s) and the title of the work, journal citation and DOI.



Martin Van Damme^{1,*} , Lieven Clarisse¹ , Bruno Franco¹ , Mark A Sutton² , Jan Willem Erisman³ , Roy Wichink Kruit⁴ , Margreet van Zanten⁴ , Simon Whitburn¹ , Juliette Hadji-Lazaro⁵, Daniel Hurtmans¹, Cathy Clerbaux^{1,5}  and Pierre-François Coheur¹ 

¹ Université libre de Bruxelles (ULB), Spectroscopy, Quantum Chemistry and Atmospheric Remote Sensing (SQUARES), Brussels, Belgium

² UK Centre for Ecology and Hydrology, Edinburgh, United Kingdom

³ Institute of Environmental Sciences, Leiden University, Leiden, The Netherlands

⁴ National Institute for Public Health and the Environment (RIVM), Bilthoven, The Netherlands

⁵ LATMOS/IPSL, Sorbonne Université, UVSQ, CNRS, Paris, France

* Author to whom any correspondence should be addressed.

E-mail: martin.van.damme@ulb.ac.be

Keywords: ammonia (NH₃), trends, emission, agriculture, biomass burning, IASI, satellite

Abstract

Excess atmospheric ammonia (NH₃) leads to deleterious effects on biodiversity, ecosystems, air quality and health, and it is therefore essential to monitor its budget and temporal evolution. Hyperspectral infrared satellite sounders provide daily NH₃ observations at global scale for over a decade. Here we use the version 3 of the Infrared Atmospheric Sounding Interferometer (IASI) NH₃ dataset to derive global, regional and national trends from 2008 to 2018. We find a worldwide increase of 12.8 ± 1.3 % over this 11-year period, driven by large increases in east Asia (5.80 ± 0.61 % increase per year), western and central Africa (2.58 ± 0.23 % yr⁻¹), North America (2.40 ± 0.45 % yr⁻¹) and western and southern Europe (1.90 ± 0.43 % yr⁻¹). These are also seen in the Indo-Gangetic Plain, while the southwestern part of India exhibits decreasing trends. Reported national trends are analyzed in the light of changing anthropogenic and pyrogenic NH₃ emissions, meteorological conditions and the impact of sulfur and nitrogen oxides emissions, which alter the atmospheric lifetime of NH₃. We end with a short case study dedicated to the Netherlands and the ‘Dutch Nitrogen crisis’ of 2019.

1. Introduction

Ammonia (NH₃) is the most abundant alkaline component of our atmosphere. Agricultural activities are responsible for the majority of its emissions [1], with volatilization from livestock manure and losses from synthetic fertilizer application accounting for over 80 % of the total emissions in, e.g. Europe [2], United States (U.S.) [3] and China [4]. For 2015, the Emission Database for Global Atmospheric Research (EDGAR) v5.0 reports a global emission total of 49.1 Tg NH₃, with 85.7 % originating from agriculture [5, 6]. Other sources include oceans and soils, waste water treatment, wild animals, human excreta, traffic and biomass burning [1, 7]. The latter was estimated to amount to 4.9 Tg in 2015 by the Global Fire Emissions Database (GFED) v4.1 s [8]. Recently, emissions from industry have also been identified as

an important and largely underestimated source of atmospheric NH₃ [9].

High NH₃ levels negatively affect ecosystems by depleting biodiversity and degrading soil and water quality [10, 11]. Atmospheric NH₃ has a remarkable short atmospheric lifetime of the order of hours [9, 12]. Once emitted, a large part of NH₃ is rapidly deposited on terrestrial and aquatic ecosystems, resulting in adverse acidifying and eutrophying effects [13, 14]. In combination with nitrogen (NO_x) and sulfur oxides (SO_x), NH₃ plays a significant role in fine particulate matter (PM_{2.5}) formation and related health impacts [15, 16]. Its contribution to PM_{2.5} formation is however still underexposed (e.g. [17–19]) and, as regulations are mostly geared towards restricting NO_x and SO_x emissions, the world is currently ‘ammonia-rich’ [20]. In Europe, China and the U.S. in particular, reduction in emissions of

nitrogen and sulfur oxides have demonstrably resulted in an increased amount of atmospheric gas-phase NH_3 during the last decade [21–24]. Several studies have concluded that reducing NH_3 emissions would be a cost-effective strategy to reduce $\text{PM}_{2.5}$ concentrations [17, 25]. It has been estimated that a 50 % reduction of the NH_3 emissions in northwestern Europe would lead to a 24 % reduction in the $\text{PM}_{2.5}$ concentration [26]. In China, the same reduction rate on NH_3 emissions, joined with a 15 % reduction on NO_x and SO_x emissions, would reduce $\text{PM}_{2.5}$ pollution by 11 %–17 % and nitrogen deposition by 34 %, but would worsen acid rain [27]. Through its role in aerosol formation and the impact of its deposition on plant productivity and carbon uptake, NH_3 also affects climate [28, 29].

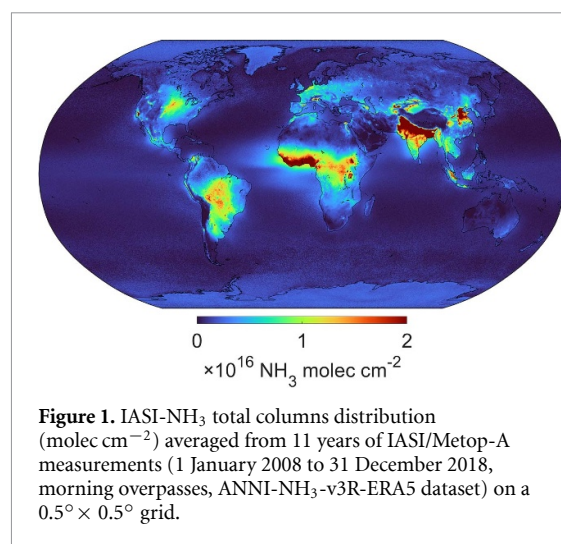
For the first decade of the 21st century, the EDGAR emissions model reports a 20 % increase of the global NH_3 emissions, but with large variations at regional and national scales [30]. Countries in Europe have committed to modest reductions of NH_3 emissions in the framework of the Gothenburg Protocol, which is part of the convention on Long-Range Transboundary Air Pollution (LRTAP) and the National Emissions Ceilings (NEC) Directive [31]. The success of this and other ammonia-control initiatives has traditionally been difficult to assess as the uncertainty in NH_3 emissions is the largest among all pollutants [1, 5]. For more than a decade now, satellite missions offer global observations of NH_3 abundance [32–35]. In particular, satellite-based datasets have already been used to identify and quantify main NH_3 point sources [9, 12, 36], to derive first changes in atmospheric NH_3 [37, 38], to constrain deposition flux estimates [39–41] and, recently, to perform inverse modeling of NH_3 emissions [42, 43].

The present study uses the reanalyzed NH_3 dataset recently obtained from the Infrared Atmospheric Sounding Interferometer (IASI) satellite over 11 years (2008–2018) to derive decadal trends throughout the world. In the next section, the satellite data are presented along with the method to derive trends and associated uncertainties. In section 3, these trends are presented, discussed and interpreted at global, regional and national scales. In the last section, a special focus is given to the case of the Netherlands, a country that received a lot of attention end of 2019 due to the ‘Dutch Nitrogen crisis’ which substantially affected the national economy [44].

2. Data and methods

2.1. Satellite measurements

Even though IASI’s main goal is to provide temperature and humidity measurements for improved weather forecasts, its instrumental characteristics enable global bi-daily measurements of a series of atmospheric constituents. In particular, its relatively high spatial resolution (12 km at nadir), scanning



mode (2100 km swath) and good spectral performance (0.5 cm^{-1} spectral resolution apodized and low radiometric noise) [45] have proven to be most useful for characterizing the spatiotemporal variability and budget of NH_3 [9, 32, 46–51]. The IASI mission consists of a suite of three identical instruments embarked on the Metop-A, -B and -C platforms, launched in 2006, 2012 and 2018, respectively. Together, these provide consistent global satellite measurements, allowing us to derive trends at global, regional and national scale. Eleven years of morning overpass IASI/Metop-A measurements have been considered here for the calculation of the global trends, while merged IASI/Metop-A (2008–2018) and -B (2013–2018) data have been used for the case study over the Netherlands. Only morning observations have been kept as their uncertainties are lower thanks to a more favorable thermal state of the atmosphere for the remote sensing of its lowest layers [46, 47].

We used version 3 of the IASI- NH_3 dataset, which was built using the ANNI (artificial neural network for IASI) retrieval framework. ANNI has been developed to perform global retrievals of NH_3 [52, 53] and was recently expanded to retrieve several other trace gases (e.g. [54–56]). Two IASI- NH_3 datasets are available: a near-real time dataset, for which the retrieval relies on meteorological information directly obtained from the IASI measurements [57] and a reanalyzed dataset that is based on data from the European Centre for Medium-Range Weather Forecasts (ECMWF) climate reanalysis [58]. The latter, named ANNI- NH_3 -v3R-ERA5, has been developed specifically for trend studies and is the one used here. Its 2008–2018 globally averaged distribution is shown in figure 1. Note that the satellite NH_3 values are reported as total columns, representing the total number of NH_3 molecules in a column from the ground surface to the top of the atmosphere expressed per unit of surface.

The general NH_3 retrieval algorithm is detailed in [52–54]. A description of the changes that were

implemented for version 3 is provided in appendix A. A careful analysis of the initial dataset revealed some spurious trends and offsets in the long-term trends over remote oceans. These included (a) two offsets that coincide with changes to the instrument, (b) a slow decreasing trend most likely due to increasing CO₂ concentrations and (c) a residual dependence on H₂O. Therefore, for the final version of the product, several debiasing procedures were applied (see again appendix A). The only potential remaining source of temporal inhomogeneity stems from the use of the IASI near real-time cloud detection algorithm, as currently no official reanalyzed cloud product is available. This most notably affects observations over the Southern Ocean and South Pacific Ocean before 2011 [59]. IASI-NH₃ measurements have been compared with ground-based and airborne independent observations in [60, 61]. More recently, a dedicated validation study was performed for version 3 of the product. A good correlation was found between in-situ vertical profiles and IASI-NH₃ total columns for both v3 datasets, with slightly better statistics for the reanalysis than for the near-real time product [62].

2.2. Trend analysis method, figures and tables

To determine the NH₃ trends and their uncertainty, the method developed by Gardiner *et al* [63] has been applied to the IASI observational time series. It relies on least squares regression and bootstrap resampling [64] to fit daily time series data to the following function:

$$\text{NH}_3(t) = ct + \sum_{n=0}^3 [a_n \sin(2\pi nt) + b_n \cos(2\pi nt)]. \quad (1)$$

The first term in this equation characterizes the long-term linear trend in the data, with the sought-after annual trend c . The other terms constitute a third-order Fourier series representing the periodic seasonal variations. This statistical method provides separate 2σ (or $p = 0.05$) lower and upper bound uncertainties of the trend values, but as the differences between both are very small, we used similarly to [63] the mean uncertainty. Following the nomenclature of that paper too, we call trends ‘significant’ if the change in NH₃ total columns exceeds their uncertainty (i.e. is significantly different from zero). Trends were computed at grid cell, country, regional and global scales in absolute (in molec cm⁻² yr⁻¹) terms. From these, we calculated total relative changes from 2008 to 2018 (i.e. the relative decadal NH₃ changes with respect to 2008, in % 10yr⁻¹) and average yearly relative trends assuming compound change rates (in % yr⁻¹). All uncertainties on the trend numbers, relative or absolute, have been reported with two significant figures.

The global distribution of the NH₃ trends at 0.5° × 0.5° resolution (56 km × 56 km at the equator) is shown in figure 2(a) in absolute value. Here the trend calculation was applied on each grid

cell separately. The same figure is shown (figure B1) but with stippled cells for non-significant trends. The national trends presented in tables 1 and B1 and in figure 2(b) were computed based on the daily average time series at the national scale. Examples of such daily time series are given in appendix B, figure B3. These figures also show separately the linear and periodic terms of the fit, together with a standard ordinary least squares regression fit. Trends calculated with the latter were generally found to be in good agreement with the trends calculated with the more robust bootstrapping method. For selected countries we show in figure 3 yearly normalized NH₃ time series which were calculated from daily averages. Global and subcontinental trends (table 1, figures 2(c) and B2) have been calculated based on the national numbers, weighted by the area of each country. In figures 2(b) and (c), countries or subcontinents with non-significant trends in atmospheric NH₃ have been hatched. These thus correspond to regions where either the uncertainty on the trend is too large or where the estimated trend is close to zero.

Apart from IASI-derived trends, we also obtained trends based on yearly emission from the aforementioned EDGAR bottom-up emission inventory (for 2008–2015) and the GFED inventory for pyrogenic NH₃ emission (2008–2018). These were calculated using a standard least squares linear regression fit and are shown in appendix B, figures B4 and B5.

3. Global, regional and national trends

East Asia stands out as the region in the world with the largest increase over 2008–2018 with a decadal increase of 75.7 ± 6.3 % and an annual growth rate of 5.80 ± 0.61 % yr⁻¹, mostly due to increases observed in the North China Plain and the Chengdu (Sichuan, China) area (figures 2(a) and B1). For China as a whole, we estimate an annual trend of 6.25 ± 0.68 % (figure 2(b)) and a decadal change of 83.3 ± 7.0 %. The increased columns are likely driven by a rise in emissions, which [4] and [65] estimated to be 1.9 and 1.7 % yr⁻¹ over 2000–2015 and 2008–2016, respectively. While agriculture still contributes to over 80 % of the emissions, recent emission-based [65] and satellite-based [9] studies have pointed out the increasing importance of non-agricultural sources, especially of industrial emitters. The contribution of fossil-fuel combustion sources, including traffic, has been lately highlighted especially during severe haze episodes [66–68]. Surprisingly, as shown in figure B4, the EDGAR v5.0 global database [6] reports a moderately slow decline in emissions over eastern China during the 2008–2015 period, which appears to be mostly due to a sharp decline in the estimates of the year 2014 and which is not observed in the satellite data. Other studies also reported relative stable emissions during the past decade (e.g. [69]).

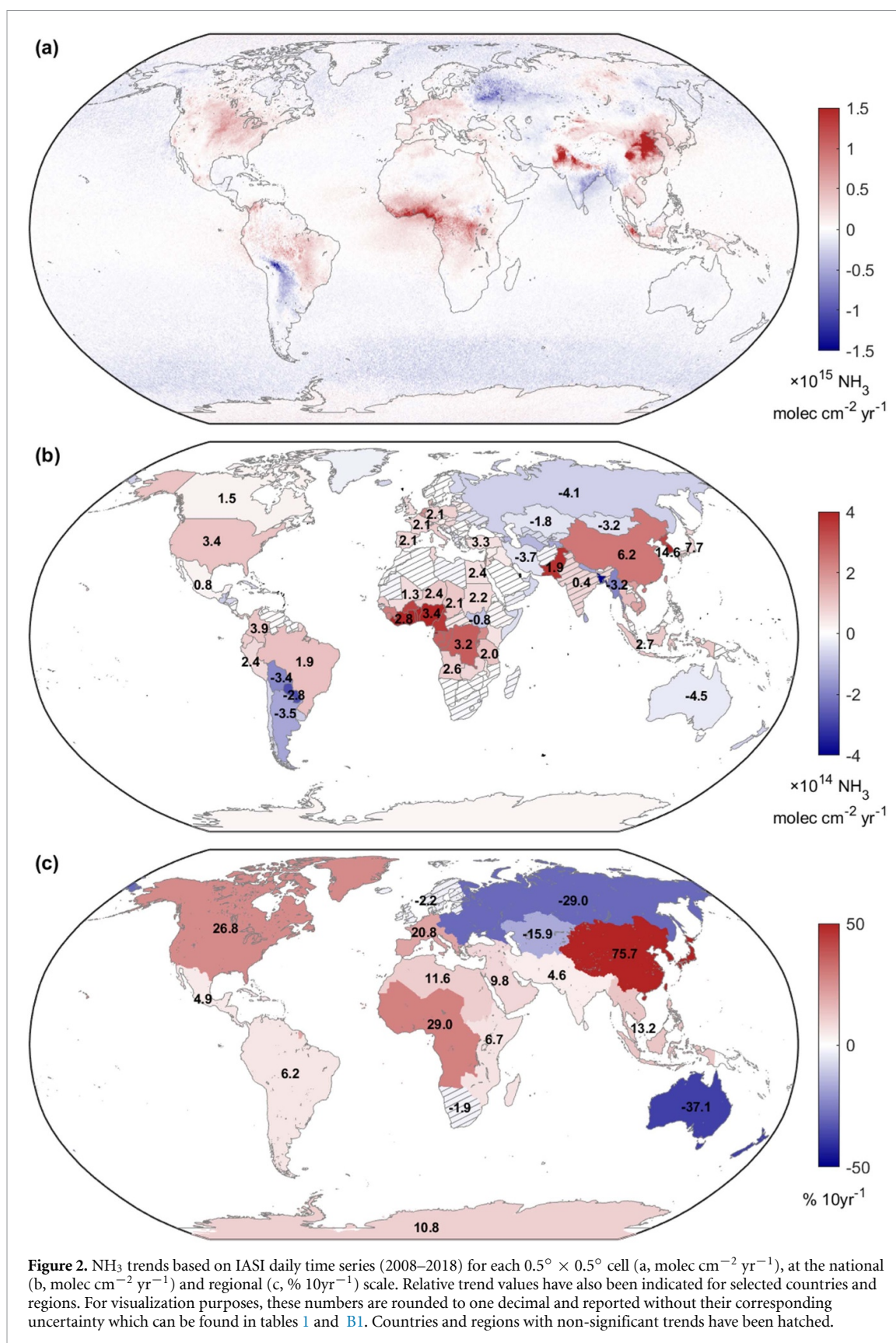


Figure 2. NH_3 trends based on IASI daily time series (2008–2018) for each $0.5^\circ \times 0.5^\circ$ cell (a, $\text{molec cm}^{-2} \text{yr}^{-1}$), at the national (b, $\text{molec cm}^{-2} \text{yr}^{-1}$) and regional (c, $\% 10\text{yr}^{-1}$) scale. Relative trend values have also been indicated for selected countries and regions. For visualization purposes, these numbers are rounded to one decimal and reported without their corresponding uncertainty which can be found in tables 1 and B1. Countries and regions with non-significant trends have been hatched.

NH_3 columns are affected both by changes in sources and sinks. For China in particular, the large increases observed by IASI after 2013 (figure 3(a)) are also likely caused in part by a longer atmospheric lifetime of NH_3 , linked to a decrease of emissions of acidifying compounds (mostly SO_x and NO_x ; e.g.

[24, 70]) following China's Clean Air Action in 2013 [69]. Despite the decline in the emissions of sulfur and nitrogen oxides, China is still facing major air quality issues and has only recently started to dedicate efforts to mitigate NH_3 emissions [27]. North and South Korea present the largest relative positive growths at

the national scale (14.7 ± 4.6 and 14.6 ± 3.6 % yr⁻¹, respectively) in Asia, followed by Japan (7.7 ± 3.3 % yr⁻¹). While anthropogenic NH₃ emissions have increased by around 1.5 % yr⁻¹ in South Korea according to the OECD [71] and EDGAR database [6], the much larger relative growth estimated for these countries may also be linked in part to an increasing eastward transport of atmospheric NH₃ from China, as previously shown for particulate matter [72, 73] and dust [74]. In excess conditions, NH₃ atmospheric lifetime can be larger than a few hours and up to a few days (e.g. [9] and references therein and [50]).

After South Korea, Pakistan exhibits the highest absolute trend of Asia. Agriculture in this country is characterized by low and declining nitrogen use efficiencies due to excessive application of synthetic fertilizers [75]. Shahzad *et al* [76] highlighted how nitrogen use and surplus increased at much faster rates than the production yield during the 1961–2014 period. This overconsumption of synthetic fertilizers in Pakistan leads to a significant increase of NH₃ in the atmosphere [77]. Its neighboring country India is as a whole characterized by a non-significant trend close to zero (0.39 ± 0.49 % yr⁻¹) but it is important to recognize that this is due to a contrasted pattern with a high upward trend in the Indo-Gangetic Plain and in the northwestern part of the country in general, while the southeastern part shows decreasing NH₃ columns (figure 2(a)). Similar results were found with the previous version of the IASI-NH₃ product over the 2008–2016 period [78]. In the last decade, India has undertaken several measures to reduce nitrogen pollution. In 2015 for instance, the government forced urea manufacturers to produce urea coated with neem oil, a natural nitrification inhibitor, to improve nitrogen use efficiency [79]. However, soil pH affects the efficiency of such inhibitors and their use could also lead to enhanced NH₃ volatilization over alkaline soils [80, 81]. Interestingly, the soil pH map of India presents the same spatial patterns as the calculated trend distribution, with alkaline soils in the northwestern part of the country and more acidic soils in eastern India [82]. Obviously, further analyses are needed to assess the impact of changing nitrogen fertilizer use and consumption on NH₃ volatilization in India.

In southeastern Asia, Myanmar presents a negative trend of -3.19 ± 0.70 % yr⁻¹. A likely explanation is a decrease in biomass burning activity for the considered time period, as seen from the GFED v4.1s trend analysis (see figure B5). In contrast, the extreme NH₃ emissions from peat fires in 2015 (see figure 3(b)) artificially drive the trend distribution in Indonesia towards high positive values over the eastern part of Sumatra [50]. The spatial patterns of the NH₃ trends in Russia can also be explained to some extent by the biomass burning events that occurred

during the 2008–2018 period. This is clear from the comparison of figures 2(a) with the trends calculated from GFED (figure B5), as well as from an analysis of the time series over selected regions. The 2014 and 2018 fire episodes in the northeastern parts of Siberia in particular are responsible for the positive trends over this remote region. For example, during the summer of 2018, NH₃ emissions from fires in Russian Federation's Republic of Sakha were so large that they could be tracked down to eastern Canada [83, 84]. The negative trends reported in the western part of the country is partly due to the exceptional amounts of NH₃ released in the atmosphere by the fires around Moscow in 2010 (see figure 3(b)) [48, 85]. This single event has a pronounced impact on the downward annual rate calculated for the whole Russian Federation (-4.11 ± 0.80 % yr⁻¹), which would however, still be negative (-2.33 ± 0.48 % yr⁻¹) if the fire period (27 July–27 August 2010) is removed from the 11-year time series. Conversely, central Asia shows a significant decrease in NH₃ which does not appear to be due to a decrease in biomass burning emissions. From the IASI measurements, we estimate downward trends around -2 % yr⁻¹ in Tajikistan, Turkmenistan and Kazakhstan. Further information on on-ground activities in this part of the world are needed to confirm and interpret this evolution.

The increase in the western and southern parts of Europe is rather homogeneous with countries like Belgium, the Netherlands, France, Germany, Poland, Italy and Spain all increasing between 2 and 4.2 % yr⁻¹. As a whole, this region presents a decadal change of 20.8 ± 4.3 %. The exceptional weather conditions of 2018 in terms of temperature and drought [86] likely explain a non-negligible part of this high trend value, as confirmed for the Netherlands (see section 4 and [87, 88]). While the EDGAR emission data is not available for 2018, the reported evolution in the 2008–2015 period is not consistent with what IASI observes. In particular, the EDGAR data exhibits heterogeneous trends over Europe, with large decreases in France and Poland, and increases in the other countries, especially in Germany. These are evidently driven by the underlying country-scale data and show the limitation of bottom-up inventories that rely on country-scale statistics, which are not always calculated and reported uniformly. According to the European Environmental Agency (EEA) [89], NH₃ emissions have been decreasing in the EU-28 since 1990 with a total decline of 24 % by 2008. From that year, reported NH₃ emissions were relatively stable, with a decline of 4 % in the period 2008–2012, followed by a new increase of 3 % from 2013 to 2017 [89, 90]. In 2018, reported emissions were lower thanks to alleged reductions of emissions in Germany, Italy, Spain, France and Slovakia [2]. This is, however, inconsistent with the substantial increase in NH₃ columns that is observed from space in 2018

Table 1. Absolute ($\text{molec cm}^{-2} \text{ yr}^{-1}$), relative ($\% \text{ yr}^{-1}$) and decadal NH_3 trends ($\% 10\text{yr}^{-1}$) calculated for selected countries and regions based on national daily average time series (2008–2018) measured by IASI/Metop-A. The relative trend is expressed as compound growth rate from 2008. The regions are shown in figure 2(c). Table B1 reports trend values for each country.

	Absolute ($\text{molec cm}^{-2} \text{ yr}^{-1}$)	Relative ($\% \text{ yr}^{-1}$)	Decadal ($\% 10\text{yr}^{-1}$)
Bolivia	$(-18.1 \pm 6.7) \times 10^{13}$	-3.4 ± 1.0	-29 ± 11
China	$(24.7 \pm 2.1) \times 10^{13}$	6.25 ± 0.68	83.3 ± 7.0
India	$(0.8 \pm 1.0) \times 10^{14}$	0.39 ± 0.49	4.0 ± 5.0
Indonesia	$(10.1 \pm 5.1) \times 10^{13}$	2.7 ± 1.4	30 ± 15
Netherlands	$(2.1 \pm 1.1) \times 10^{14}$	3.6 ± 1.9	42 ± 21
Nigeria	$(49.4 \pm 7.9) \times 10^{13}$	3.38 ± 0.62	39.4 ± 6.3
Russia	$(-7.1 \pm 1.7) \times 10^{13}$	-4.11 ± 0.80	-34.2 ± 8.3
Spain	$(7.6 \pm 2.8) \times 10^{13}$	2.08 ± 0.82	22.9 ± 8.5
Turkey	$(6.0 \pm 1.4) \times 10^{13}$	3.31 ± 0.89	38.5 ± 9.3
United States	$(11.4 \pm 1.7) \times 10^{13}$	3.42 ± 0.59	39.9 ± 6.1
Northern Europe	$(-0.4 \pm 1.4) \times 10^{13}$	-0.22 ± 0.81	-2.2 ± 8.4
Western and southern Europe	$(6.7 \pm 1.4) \times 10^{13}$	1.90 ± 0.43	20.8 ± 4.3
Eastern Europe and Russia	$(-6.3 \pm 1.6) \times 10^{13}$	-3.37 ± 0.70	-29.0 ± 7.3
Northern Africa	$(2.5 \pm 1.0) \times 10^{13}$	1.11 ± 0.47	11.6 ± 4.8
Western and central Africa	$(20.3 \pm 1.6) \times 10^{13}$	2.58 ± 0.23	29.0 ± 2.3
Eastern Africa	$(30.1 \pm 8.8) \times 10^{12}$	0.65 ± 0.19	6.7 ± 1.9
Southern Africa	$(-2.9 \pm 7.6) \times 10^{12}$	-0.19 ± 0.48	-1.9 ± 4.9
Northern America	$(6.1 \pm 1.0) \times 10^{13}$	2.40 ± 0.45	26.8 ± 4.5
Central America	$(1.3 \pm 1.2) \times 10^{13}$	0.48 ± 0.44	4.9 ± 4.5
South America	$(3.0 \pm 1.7) \times 10^{13}$	0.60 ± 0.34	6.2 ± 3.5
Western Asia	$(11.4 \pm 9.6) \times 10^{12}$	0.94 ± 0.80	9.8 ± 8.3
Central Asia	$(-5.4 \pm 1.5) \times 10^{13}$	-1.72 ± 0.44	-15.9 ± 4.5
East Asia	$(20.5 \pm 1.7) \times 10^{13}$	5.80 ± 0.61	75.7 ± 6.3
South Asia	$(6.1 \pm 5.2) \times 10^{13}$	0.45 ± 0.38	4.6 ± 3.9
Southeastern Asia	$(5.3 \pm 2.4) \times 10^{13}$	1.25 ± 0.59	13.2 ± 6.1
Oceania	$(-32.7 \pm 3.8) \times 10^{12}$	-4.54 ± 0.43	-37.1 ± 4.4
Antarctica	$(21.7 \pm 3.2) \times 10^{12}$	1.03 ± 0.16	10.8 ± 1.6
Global	$(45.6 \pm 4.6) \times 10^{12}$	1.21 ± 0.13	12.8 ± 1.3

(see figure 3(a)), underlining the urgent need of taking into account meteorological factors in the current state-of-the-art bottom-up emissions inventories [1]. Declining emissions of acidifying compounds, as much as 62 % in the 2008–2018 period for SO_x and 28 % for NO_x in EU-28 [89], also increased the atmospheric lifetime of NH_3 and impacted the trend in the region [23, 91].

In the Middle East, Israel, Jordan and Turkey are characterized by relatively large positive trends over 3 \% yr^{-1} , which likely originate from increased emissions. For example, Turkey experienced an important intensification of its agricultural production during the past two decades [92]. During the 2008–2018 period, agricultural use of nitrogen nutrients in the country grew by 2.8 \% yr^{-1} [93], similarly to Israel, while the total anthropogenic emissions increased sharply by 4.8 \% yr^{-1} [89]. While Syria shows a moderate positive trend, several grid cells around Damascus and south of Homs in figure 2 exhibit a downward trend reflecting the decline of atmospheric emissions due to the civil war that started in 2011 [12]. In northern Africa, only Tunisia and Egypt present significant positive changes in NH_3 columns. The latter, characterized by an upward trend of $2.39 \pm 0.82 \text{ \% yr}^{-1}$ due to intensive agriculture in the Nile Delta and River, is known to be the largest fertilizer

consumer in Africa and to have one of the highest nitrogen application rates in the world [94]. Elry *et al* [94] also discusses the strong increase in gaseous NH_3 emissions in 2014–2016 following the enhanced nitrogen use on croplands in the country. Figure 2(a) shows that significant increasing trends are also found along the coast of Algeria and especially Morocco, even though for these countries as a whole the trends are not significant.

Western and central Africa are characterized by a strong upward trend in atmospheric NH_3 total columns that is in absolute terms of a similar magnitude than east Asia ($(20.3 \pm 1.6) \times 10^{13} \text{ molec cm}^{-2} \text{ yr}^{-1}$), but lower in relative ($2.58 \pm 0.23 \text{ \% yr}^{-1}$) (see table 1). This region is dominated by biomass burning emissions associated with agricultural practices [95]. For example, Nigeria presents an upward trend of $3.38 \pm 0.62 \text{ \% yr}^{-1}$. Using the 2008–2017 data record from a previous version of the IASI- NH_3 dataset, a national increase of 6 \% yr^{-1} has been reported for the February–March period which was attributed to agricultural preparation in slash-and-burn cropping systems [96]. In addition, it is worth noting that the agricultural use of nitrogen nutrient in the country increased strongly by 12 \% yr^{-1} during the 2008–2018 period [93]. In eastern Africa, South Sudan stands out with

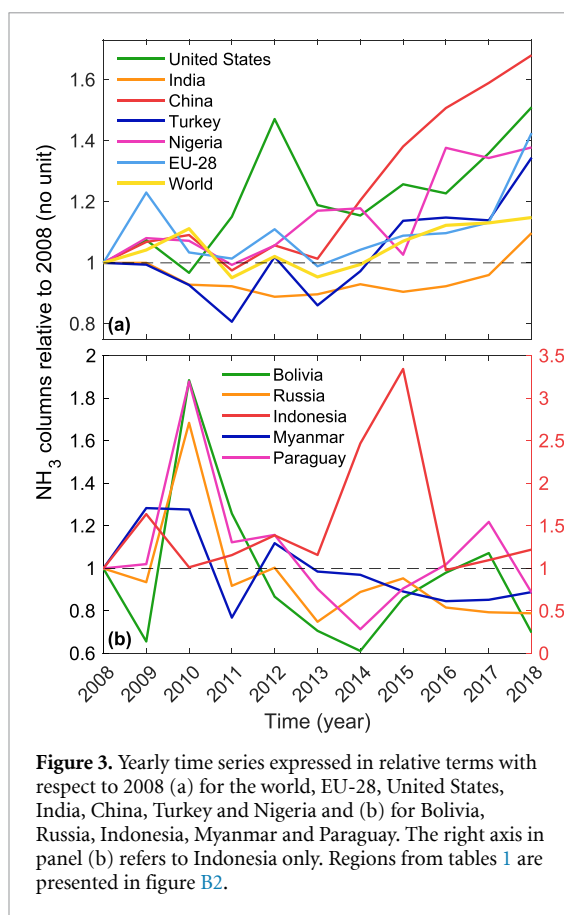


Figure 3. Yearly time series expressed in relative terms with respect to 2008 (a) for the world, EU-28, United States, India, China, Turkey and Nigeria and (b) for Bolivia, Russia, Indonesia, Myanmar and Paraguay. The right axis in panel (b) refers to Indonesia only. Regions from tables 1 are presented in figure B2.

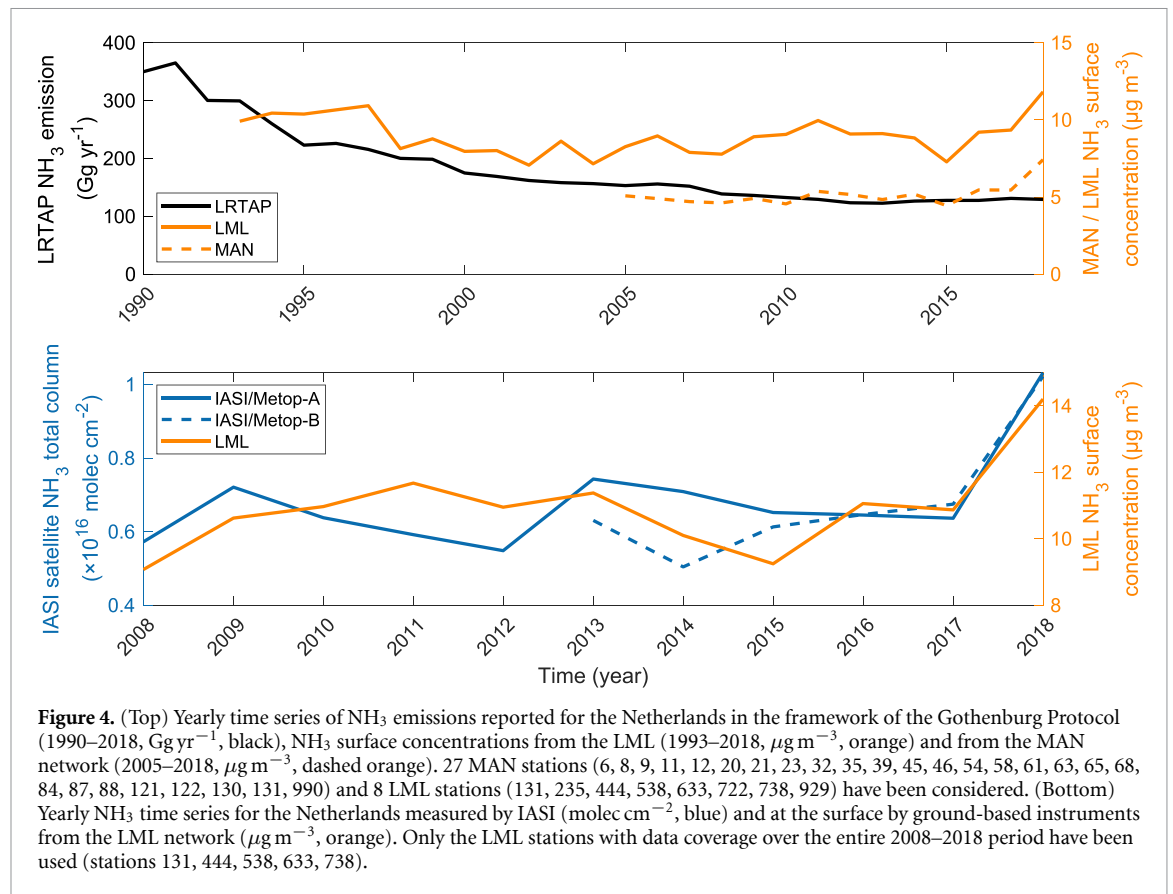
a downward trend of $-0.77 \pm 0.47 \text{ \% yr}^{-1}$. This is likely related to changes in wetland extent in the Sudd, a vast swamp located in this country [96]. The regional conflict that broke out in 2013 also drastically affected agricultural activities, with a cereal production reduced by 25 % in 2017 and a drop in livestock populations [97, 98]. The entire eastern Africa presents a very slight upward trend likely driven by increased pyrogenic emissions in the northeastern part of Democratic Republic of the Congo and in the southwestern part of Ethiopia.

The relatively small decadal change in NH_3 total columns reported in South America ($6.2 \pm 3.5 \text{ \%}$) hides regional and national disparities (figure 2). The northwestern coastline, extending from Venezuela to Peru, is the region with the largest positive rates. This is also seen in the EDGAR derived trends, for which these increases relate to agricultural emissions. The growing poultry production along the Peruvian coast is for instance well documented [9]. The positive trend in Brazil is the result of more intense pyrogenic emissions in the central part of the country and, according to EDGAR, increases in anthropogenic emissions in the southeastern region around Sao Paulo (see figure B4). Jankowski *et al* [99] also describes how intensification of the Amazon agriculture worsens nitrogen pollution. Bolivia and Paraguay exhibit negative trends around -3 \% yr^{-1} related to important biomass burning episodes that occurred in 2010 (figures 3(b) and B5).

In the U.S., IASI NH_3 columns rose by $3.42 \pm 0.59 \text{ \% yr}^{-1}$. This result is in line with the trends obtained from the AIRS satellite (2.6 \% yr^{-1} over 2002–2016 [37]) and from ground-based measurements (e.g. [21]). Modeling studies have provided evidence that the upward trend of gas-phase NH_3 in the U.S. is partly due to reduced SO_x and NO_x emissions [100, 101]. However, it has also been shown that changing meteorological factors (e.g. drought, temperature) play a role in the increase of NH_3 concentrations in the region [101, 102]. Reported national emissions decreased from 2008 to 2014 by 3.4 \% yr^{-1} , but showed an upturn in the following years to reach the same level in 2017–2018 as in 2008 [103]. At the state scale, the National Emissions Inventory (NEI) from the Environmental Protection Agency (EPA) reports a generally increasing emission trend in the western states, but a declining trend in the central-eastern states [104]. Satellite observations present nonetheless a positive trend over the entire country (figures 2(a) and (b)). The peak in 2012 in figure 3(a) could be related to higher temperatures in the summer and a related increase in NH_3 volatilization from soils, as reported for NO_x soil emissions [101]. At present, NH_3 plays a key role in nitrogen deposition in the country (contributing up to 65 % in some places), and these deposition fluxes will be difficult to mitigate without reducing emissions [105]. A significant positive trend of $1.53 \pm 0.83 \text{ \% yr}^{-1}$ is also measured in Canada (note that Yamanouchi *et al* [106] recently reported a trend of $8.38 \pm 0.77 \text{ \% yr}^{-1}$ at the city scale of Toronto using the same IASI dataset). While the national emission inventory reports more or less constant anthropogenic emissions over the 2008–2018 period [107], biomass burning sustains the increasing trend in NH_3 total columns at northern latitudes [108, 109]. EDGAR presents a pronounced discontinuity between the trend reported for the U.S. and Canada (figure B4).

The calculated trends for Australia are in relative terms quite large at $-4.53 \pm 0.45 \text{ \% yr}^{-1}$. It is however important to note that in absolute terms this decline is almost negligible and artificial. In fact, inspection of figure 2 shows declines below $0.5 \times 10^{15} \text{ molec cm}^{-2} \text{ yr}^{-1}$ in most of the Southern hemisphere at the latitude of Australia. These could be related to the misclassification of clouds during the early 2008–2018 period (see section 2.1 and [59]), or due to an imperfect CO_2 trend correction (see appendix A). For the same reason, trends in Argentina, Chile and South Africa are to be interpreted with caution. The trends over the ice sheets of Antarctica and Greenland are spurious, and exacerbated by the general poorer performance of the NH_3 retrieval over cold surfaces (see again appendix A).

From the national trends we have calculated a worldwide decadal increase in atmospheric NH_3 total columns of $12.8 \pm 1.3 \text{ \%}$, which corresponds to a positive growth rate of $1.21 \pm 0.13 \text{ \% yr}^{-1}$. Note that



these numbers are for land only. Trends over coastal areas follow in general those observed over the nearby land regions located upwind. For example, a significant positive trend in transported NH₃ is clearly identifiable in the Gulf of Guinea (southern coast of western Africa), in the Yellow Sea (east coast of China) and in the Caribbean Sea (northern coast of Colombia). Conversely, following the decline in NH₃ total columns observed in southeastern India, a negative trend is calculated over the Bay of Bengal and the Arabian Sea.

4. Case study: the Netherlands

The Netherlands was one of the first countries worldwide to implement NH₃ abatement measures in the 1980s. This included regulation of manure application rates, introducing the mineral accounting system, introduction of emission poor housing systems, manure storage coverage and injection of manure in the soil. Since the early 1990s, NH₃ is measured hourly at eight locations in the country from the ground-based stations of the National Air Quality Monitoring Network (or LML standing for ‘Landelijk Meetnet Luchtkwaliteit’), which was set up to monitor the Dutch NH₃ emissions abatement policies [22, 110]. In 2005, the LML network was extended by measurements with passive samplers in the Measuring Ammonia in Nature (MAN) network to follow the NH₃ concentrations in nature areas [111, 112].

More than 20 years ago, a discrepancy was observed between these NH₃ measurements and expected levels derived from estimated NH₃ emissions in the Netherlands [113]. Different reasons were found for this mismatch: (a) a changing chemical climate which affected the conversion rate of NH₃ to NH₄⁺; (b) a reduction of acidifying compounds such as SO₂ and NO_x both in the atmosphere as well as on the surface leading to more NH₃ in the atmosphere; (c) less effective abatement measures in practice as compared to measured lab reductions; (d) fraud with manure transports and (e) the contribution of unknown sources such as the sea and the senescence of leaves [114–116].

LML NH₃ concentrations measured at the surface show a downward trend of 36 % for the 1993–2004 period, while an upward trend of 19 % is reported for 2005–2014 [22]. In contrast, the official NH₃ emissions reported in the framework of the Gothenburg Protocol decreased for the entire period in the Netherlands and are currently 63.1 % lower than in 1990, even though since 2010, these have leveled off [89]. This is illustrated in the top panel of figure 4 which shows the evolution of the reported emissions (1990–2018, Gg yr⁻¹, black) as well as yearly NH₃ surface concentrations from the LML (1992–2018, µg m⁻³, orange) and the MAN network (2005–2018, µg m⁻³, dashed orange). van Zanten *et al* [22] have shown that the comparison between the emission and concentration trend improves when

the influence of meteorological conditions on the concentrations is taken into account.

Using 11 years (2008–2018) of IASI satellite daily observations of NH_3 columns, we calculate an increasing trend of $3.6 \pm 1.9 \text{ \% yr}^{-1}$ in the Netherlands. Over the same time-period, the daily ground-based NH_3 concentrations measured at five LML sites exhibit a consistent $2.5 \pm 0.5 \text{ \% yr}^{-1}$ growth rate. The bottom panel of figure 4 presents the annual NH_3 time series for IASI/Metop-A (molec cm^{-2} , blue), IASI/Metop-B (molec cm^{-2} , dashed blue) and LML ($\mu\text{g m}^{-3}$, orange). A sharp increase in the annual mean is measured in 2018, due to the exceptionally warm, sunny and dry weather conditions during that year, as NH_3 volatilization strongly increases with temperature and as deposition rates are lower when it is drier [1, 86–88].

In 2018, the European Court of Justice advised that the current Dutch legislation was not strict enough to protect Natura 2000 areas from nitrogen deposition [117], as required by the European Habitat Directive (EHD) (directive 92/43/EEG). This led to several rulings by the Dutch Council of State in 2019, putting on hold more than 18 000 projects on building houses and roads and in the agricultural sector and thus leading to the ‘Dutch Nitrogen crisis’. The proposed policy to halve the country’s livestock population to reduce nitrogen deposition caused massive demonstrations from farmers [44]. A special commission was put in place, the Commission Remkes, to advise about the long-term policies to reduce nitrogen. They recommended that emissions should be reduced by 50 % in 10 years to protect 75 % of the Natura 2000 against excess nitrogen deposition and that on a local scale, further reductions are necessary.

5. Conclusions

Using the data record from the IASI sounder we have obtained and characterized the evolution of atmospheric NH_3 at global, regional and national scales from 2008 to 2018. We have reported large increases of NH_3 in several subcontinental regions over the last decade, especially in east Asia ($75.7 \pm 6.3 \text{ \%}$) but also in western and central Africa ($29.0 \pm 2.3 \text{ \%}$), North America ($26.8 \pm 4.5 \text{ \%}$) and western and southern Europe ($20.8 \pm 4.3 \text{ \%}$). The upward trends observed in many countries can be attributed to a combination of increasing emissions and a longer residence time of NH_3 in the atmosphere due to declining emissions of sulfur and nitrogen oxides. Regions dominated by biomass burning emissions exhibit decreasing or increasing trends depending on when the strongest events took place. Apart from declines related to fires, notable declines were also found in the southwestern part of India and central Asia.

In view of the major role of NH_3 for the loss of biodiversity, for air quality and human health, emissions need to be reduced urgently. A series of

options exists to control the loss of NH_3 from agricultural activities to the atmosphere (e.g. [118]). Limiting these atmospheric NH_3 losses would also have co-benefits for our climate [119]. Recent studies have shown that the abatement costs to reduce NH_3 emissions is much lower than the economical and societal benefits (see [120] for Europe and [121] for China), which should trigger our willingness for action. Current and planned infrared satellite missions provide the necessary observational means to monitor the effect of implemented policies (e.g. [122, 123]) to support the goals of the Sustainable Nitrogen Management resolution (UNEP/EA.4/Res.14) adopted by the United Nations Environment Assembly on 15 March 2019 [124].

Data availability statement

The IASI- NH_3 datasets are available from the Aeris data infrastructure (<http://iasi.aeris-data.fr/NH3>). It is also planned to be operationally distributed by EUMETCast under the auspices of the EUMETSAT Atmospheric Monitoring Satellite Application Facility (AC-SAF; <http://ac-saf.eumetsat.int>).

Acknowledgments

IASI has been developed and built under the responsibility of the Centre National d’Études Spatiales (CNES, France). It is flown on board the Metop satellites as part of the EUMETSAT Polar System. The IASI L1c data are received through the EUMETCast near real-time data distribution service. National and regional maps have been made with Natural Earth (naturalearthdata.com). The research was funded by the F.R.S.-FNRS and the Belgian State Federal Office for Scientific, Technical and Cultural Affairs (Prodex arrangement IASI.FLOW). M Van Damme is Postdoctoral Researcher (Chargé de Recherche) and L Clarisse is Research Associate (Chercheur Qualifié) both supported by the Belgian F.R.S.-FNRS. M A Sutton acknowledges support from the Global Environment Facility (GEF) through the UN Environment Programme for the Towards INMS project. C Clerbaux is grateful to CNES for scientific collaboration and financial support.

Appendix A. Version 3 ANNI- NH_3 product

The ANNI- NH_3 -v3 IASI product builds on the heritage of version 1 [52], version 2 [53], and recent improvements in the neural network (NN) retrieval setup introduced in Franco *et al* [54] for the retrieval of volatile organic compounds (VOCs). We refer to the above-mentioned papers for a detailed description of the retrieval methodology. The specific changes from v2.2 to v3 for NH_3 are outlined in detail below.

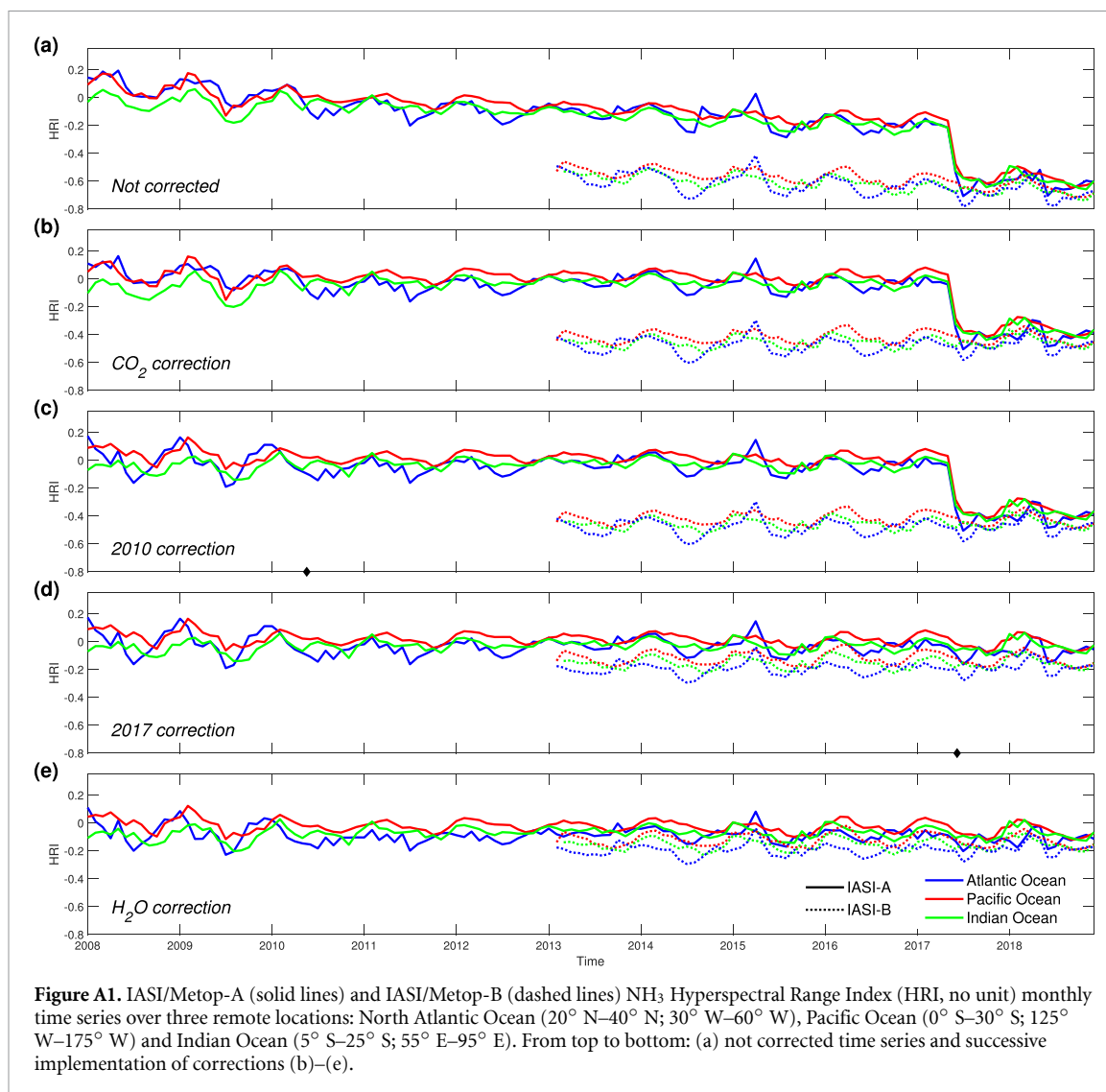


Figure A1. IASI/Metop-A (solid lines) and IASI/Metop-B (dashed lines) NH_3 Hyperspectral Range Index (HRI, no unit) monthly time series over three remote locations: North Atlantic Ocean (20°N – 40°N ; 30°W – 60°W), Pacific Ocean (0°S – 30°S ; 125°W – 175°W) and Indian Ocean (5°S – 25°S ; 55°E – 95°E). From top to bottom: (a) not corrected time series and successive implementation of corrections (b)–(e).

A.1. Changes to the HRI and debiasing procedures

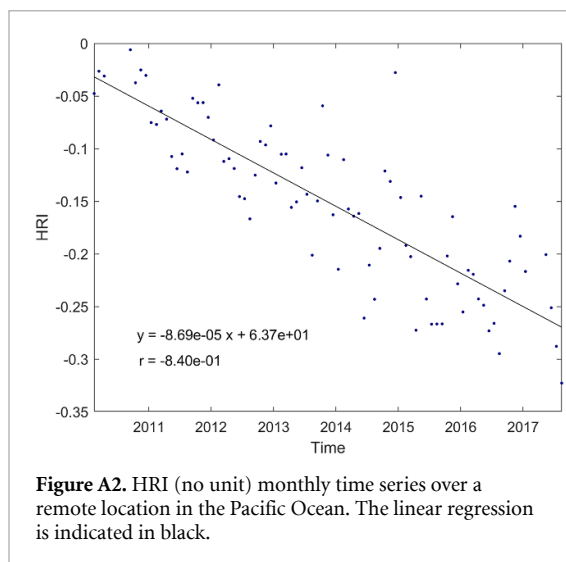
The Hyperspectral Range Index (HRI) has been set up following the iterative procedure outlined in [54]. The spectral range has been slightly reduced (812 – 1126 cm^{-1}) to minimize interferences from other species and/or local variation in surface emissivity. The end result is that the HRI is more sensitive to NH_3 and less affected by interferences.

Analysing the initial time series of the mean HRI over remote oceans, we noticed (a) offsets that coincided with changes to the IASI instrument, (b) a slowly decreasing trend and (c) a residual dependence on H_2O . In the rest of the section we outline the first order corrections that were introduced to account for all of these.

The declining trend over remote areas that was identified in the HRI of NH_3 is apparent in the top panel of figure A1. As the trend is linear, and as there are a couple of weak CO_2 absorption bands in the 812 – 1126 cm^{-1} spectral range, this trend is most likely due to the ever increasing concentrations of CO_2 . To correct this bias, we analyzed monthly averaged HRI from IASI spectra measured over a remote

location in the Pacific Ocean (17°N – 22°N ; 153°W – 158°W) versus time (figure A2). The linear regression ($y = -8.69 \times 10^{-5}x + 63.75$, $r = -0.84$, with x and y being the time (in months) and the HRI (no unit), respectively) models the relationship well and was therefore used to apply a first-order correction to the calculated HRI.

On 7 June 2017, a minor change in the configuration parameters for the apodization function of IASI/Metop-A instrument had a clear impact on the calculated HRI (figure A1, panels (a)–(c)). This recalibration made IASI/Metop-A more in line with IASI/Metop-B instrument. As the HRI is based on a covariance matrix from spectra of the year 2013, the HRI calculated after the recalibration for IASI/Metop-A have to be adjusted, as well as the entire time series of IASI/Metop-B. Comparison of the HRI values on 6 June with the ones from 8 June 2017, revealed a temperature dependence in the offset. A satisfactory correction was obtained using a linear regression ($y = -3.5 \times 10^{-3}x - 0.69$, $r = 0.89$, with x being the temperature of the baseline (in K) and y the median of the HRI difference between



the 6 and the 8 June 2017 (no unit); see figure A1, panel (d)).

Another change in the IASI Level 1C occurred on 18 May 2010 [125] and corresponds to an improvement of the spectral calibration [126]. An empirical correction was introduced as a function of latitude and day of the year. The precise offsets were computed as the difference between the median HRI calculated before and after the 18 May 2010, the median being calculated in 1° latitude bins from all the HRI with an absolute longitude above 160° and an absolute value below 5. This difference was calculated for each day of the year and applied to the HRI calculated before the 18 May 2010 (figure A1, panel (c)).

Finally, a H_2O correction similar to the one applied in the previous ANNI- NH_3 version (already described in [53]) was implemented. This does not change the behavior of the HRI over time, but helps to de-bias it (i.e. after the correction, the mean HRI over remote oceans is closer to zero). Panel (e) of figure A1 presents the corrected monthly time series of HRI over three remote locations. It shows that the corrections allow us to obtain a coherent time series over the IASI operating period, centered around zero and as expected without noticeable jumps or trends.

A.2. Changes to the neural network architecture and training

The following series of changes have been introduced:

- The size of the network was increased from one computational layer of 15 neurons [52] to two layers of 12 nodes.
- In terms of input variables, similarly to the treatment of VOCs [54], we now use a coarse H_2O profile as input to the network, as opposed to the total column that was used before. In addition, three extra temperature levels are introduced in the lower troposphere (at 0.5, 1.5 and 2.5 km above the surface). Especially in the evening, when thermal

inversion can occur, it is expected that this change results in a more accurate retrieval. Finally, the surface temperature is kept as an input parameter to the network instead of a baseline temperature used for the VOCs.

- The range of thermal contrast situations in the training set was artificially increased to better train the network. In addition, the total number of samples in the training set increased from 450 000 to close to 500 000 (also because now two networks are trained, as explained in the next point).
- Similarly to the previous versions of the NN retrieval of NH_3 , the vertical profile of NH_3 was parameterized with a Gaussian function for the forward simulations. It is now defined as:

$$\text{NH}_3(\text{vmr}) = \text{ScalFact} \cdot e^{-\left(\frac{z-z_0}{2\sigma}\right)^2}. \quad (\text{A1})$$

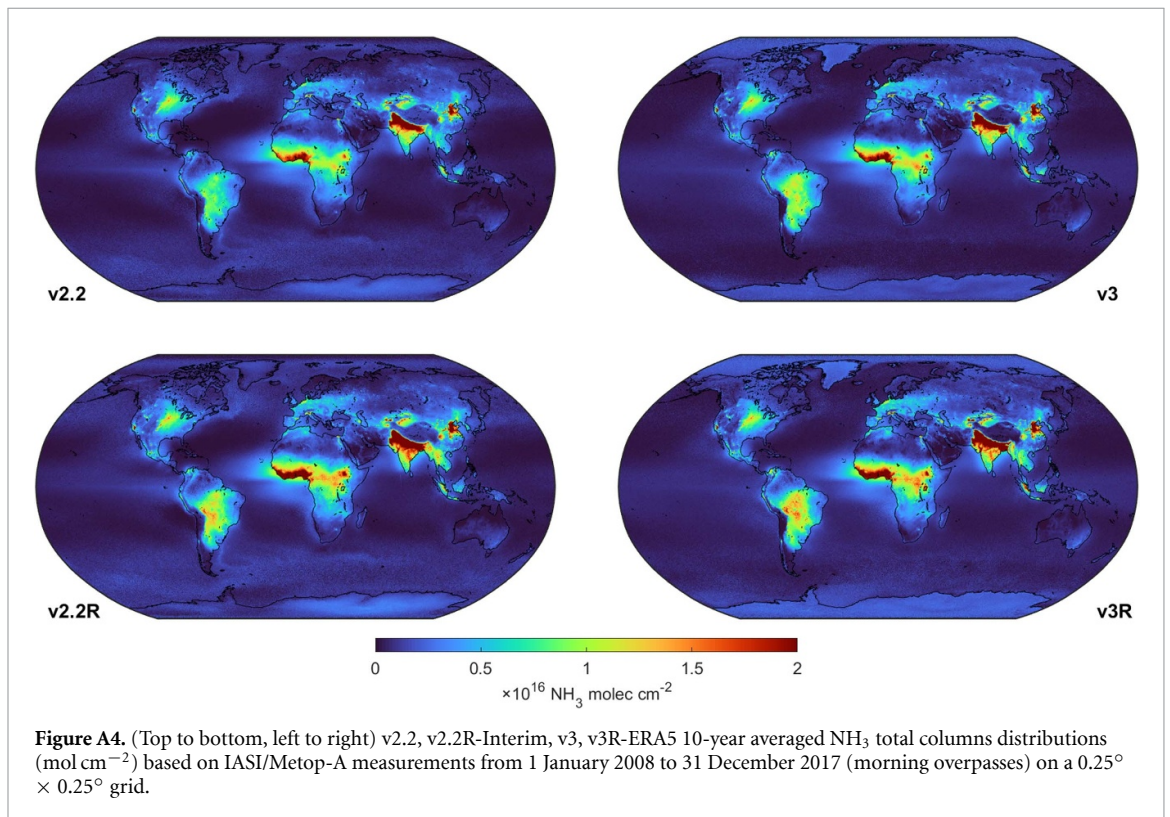
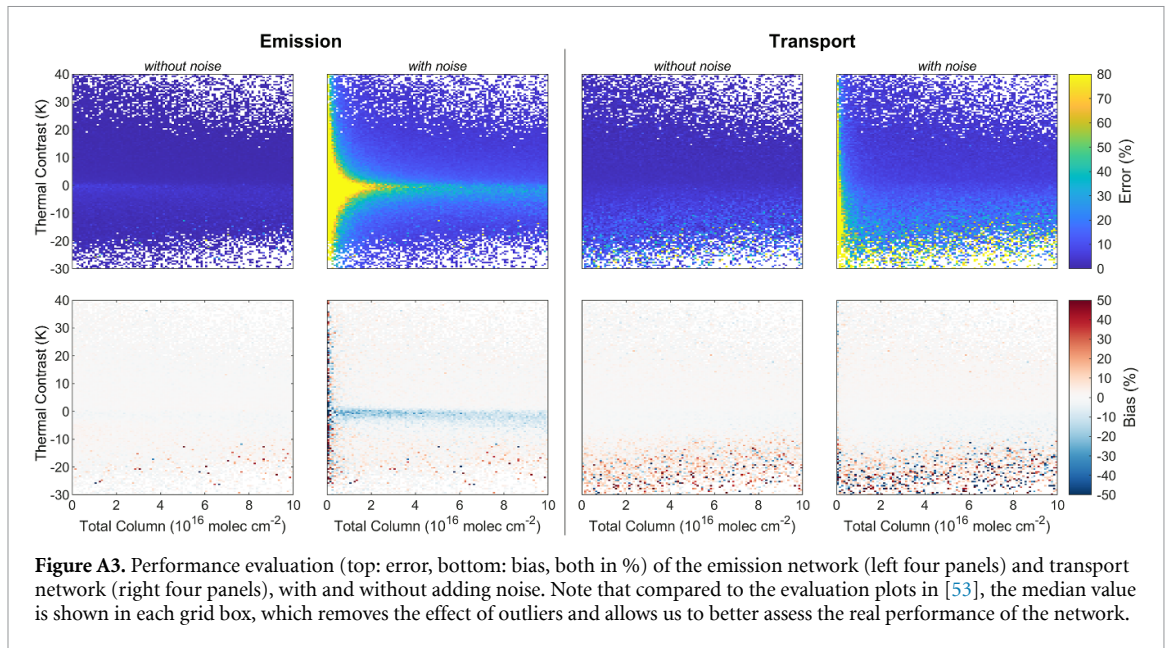
Two different training sets have been built:

- (a) One representative for observations close to emission sources (thus with the peak concentration at the surface), where z_0 was fixed to 0 km and where sigma (σ) was assigned a random number between 100 m and 6 km.
- (b) One representative for transported NH_3 , with a peak concentration above the surface. Here z_0 was assigned a random number between 0 and 20 km.

- The training performance is evaluated in figure A3 and shows similar good performances as in the previous versions.

A.3. Changes to the input data and post-filtering

- As before, IASI L2 data is used as meteorological inputs to the network, and the resulting near-real time (NRT) NH_3 product is called ANNI- NH_3 -v3. A second reanalysis product, ANNI- NH_3 -v3R, is also available. This dataset was produced with the same neural networks, but instead of the IASI L2 data, reanalyzed ERA5 data was used as meteorological inputs [58]. Note that ANNI- NH_3 -v2R still used the ERA-Interim data. ERA5, compared to ERA-Interim, has much improved meteorology and is available on an hourly timescale with a 0.28125° resolution.
- Observations above land are standard retrieved using the neural network for source areas (emission network), with as σ value the collocated ERA5 boundary layer height for v3R (see [52]). For the NRT product v3, we used as input for σ a monthly climatology based on over 10 years of ERA5 data (from October 2007 to December 2018). For observations above the ocean, we assume $z_0 = 1.4$ km and $\sigma = 1.28/\sqrt{2}$ (see again [52]).
- The condition on the ratio in the post-filter (see section 2.2 in [53]) has been returned to keep as



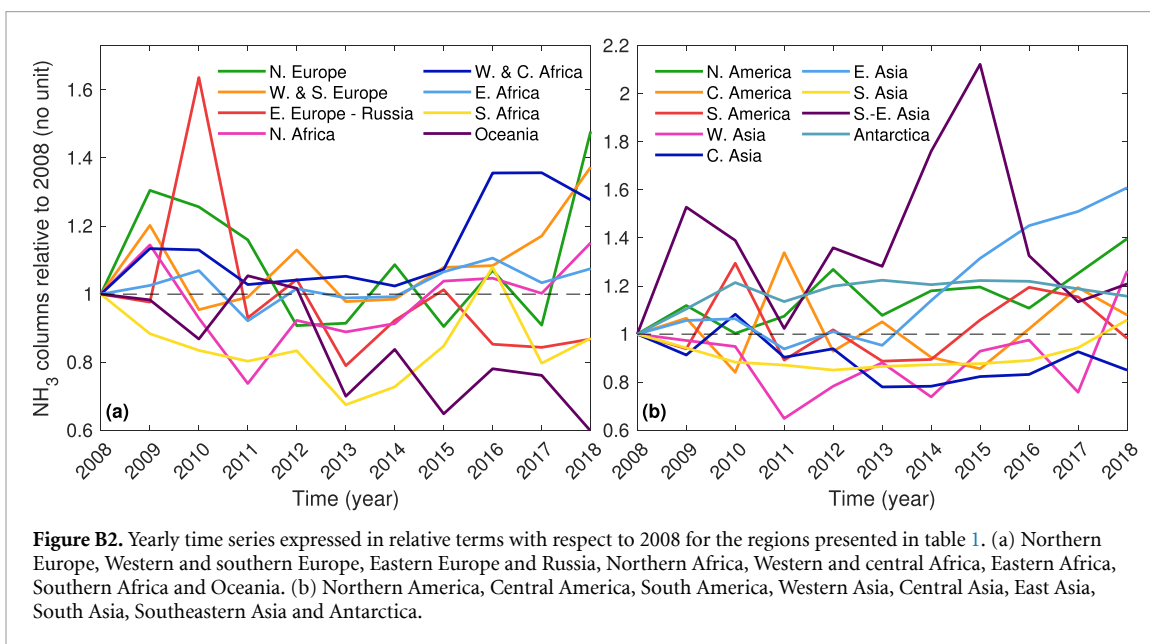
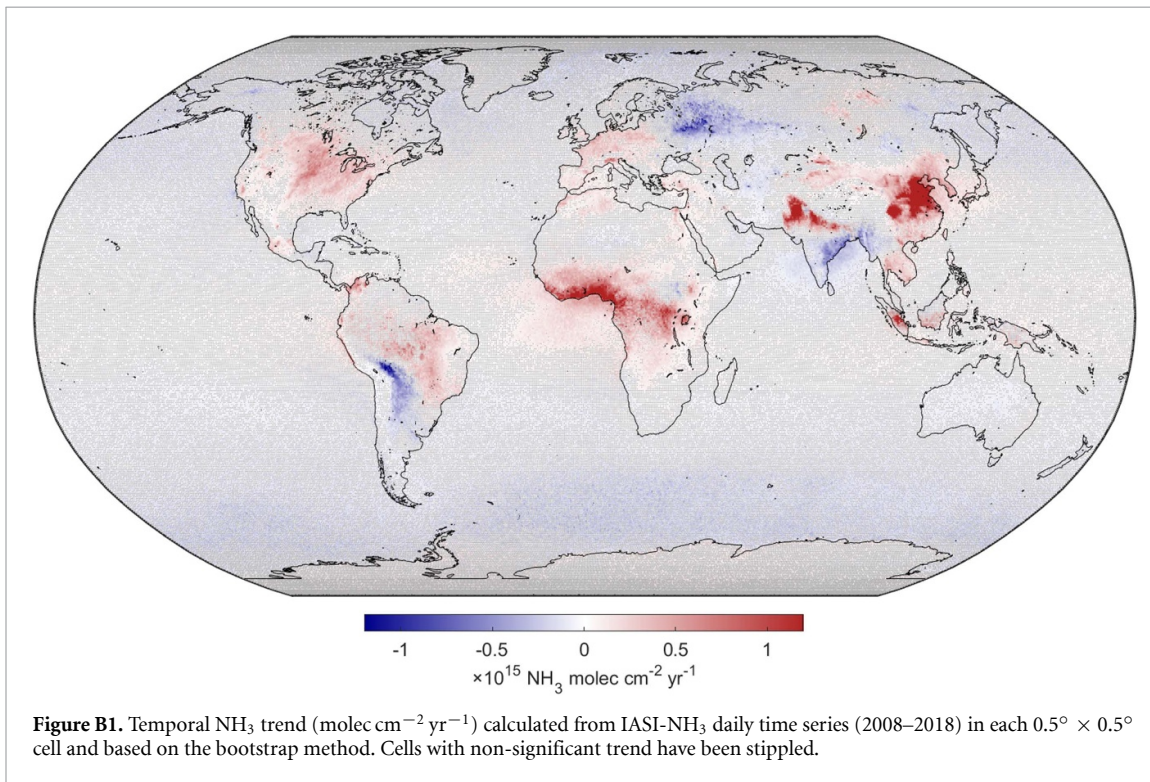
much as possible ‘good observations’, while removing those with a very large uncertainty. In particular, the threshold value on the ratio NH_3/HRI is now $1.5 \times 10^{16} \text{ mol cm}^{-2}$ instead of $1.75 \times 10^{16} \text{ mol cm}^{-2}$ (so slightly more measurements are retained).

A.4. Example

Overall and on average, the v3 does not differ significantly from v2, although differences can be large on individual observations: for columns above

$4 \times 10^{15} \text{ molec cm}^{-2}$, 80 % of the data agree to within 20 % [62]. As an illustration, figure A4 presents the IASI- NH_3 10-year averaged distributions from the four datasets (v2.2, v2.2R, v3 and v3R). The averaged columns are slightly larger in the reanalyzed versions, and higher for v3 than for v2. One notable regression in v3 is the performance over ice sheets at high latitude, which yield a larger mean NH_3 column than in v2.2. This is likely related to the fact that the current post-filter is less stringent and was tuned for the tropics and mid-latitudes.

Appendix B. Figures and tables



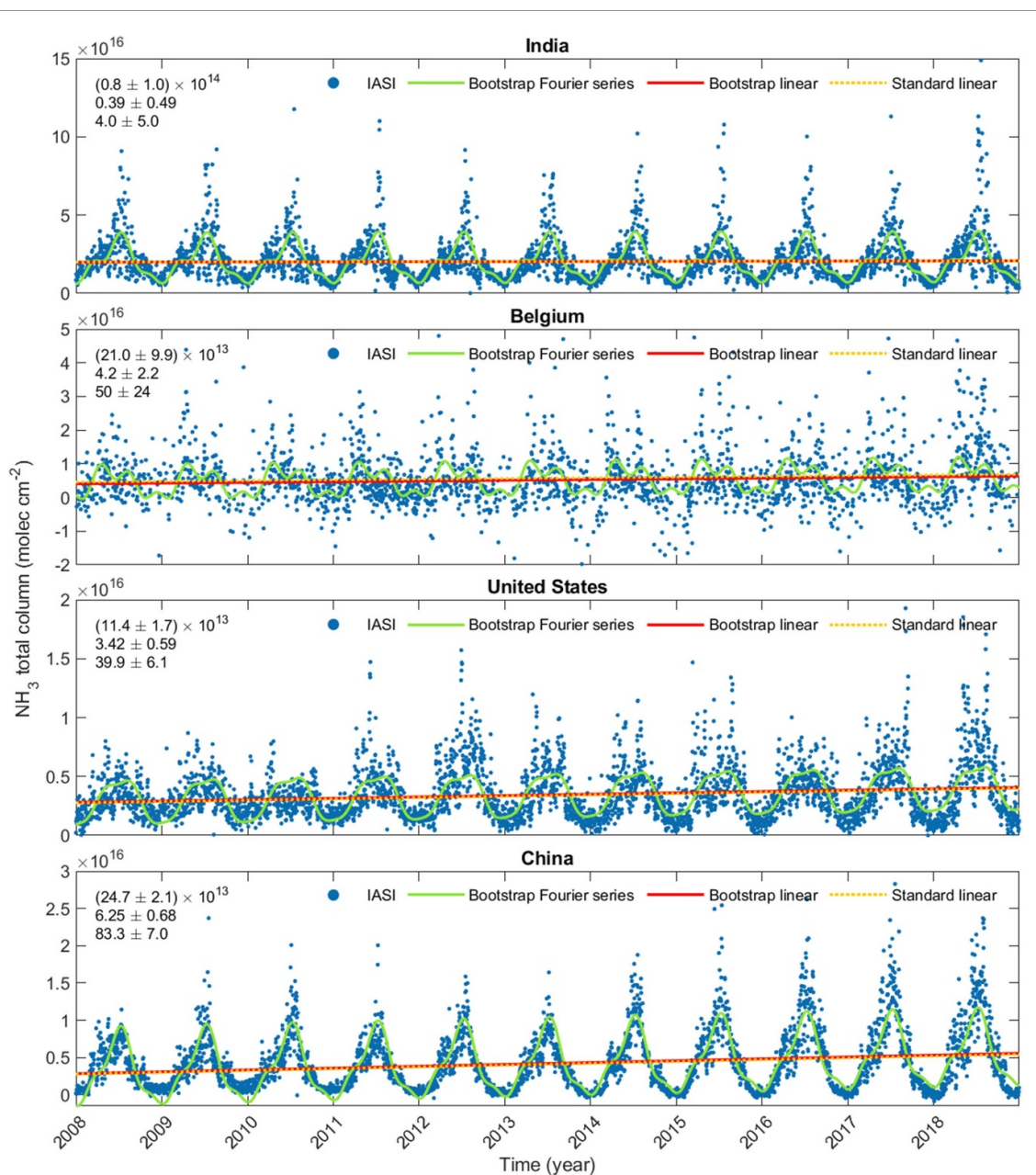


Figure B3. Bootstrap (green and red) and standard least squares linear regression (dashed yellow) fit applied on (daily and yearly, respectively) IASI- NH_3 time series (blue, molec cm^{-2}). National absolute (molec $\text{cm}^{-2} \text{yr}^{-1}$) and relative ($\% \text{yr}^{-1}$) NH_3 trend and decadal relative change ($\% 10\text{yr}^{-1}$) based on national daily time series (2008–2018) measured by IASI/Metop-A are indicated as inset in the top-left corner of each subpanel.

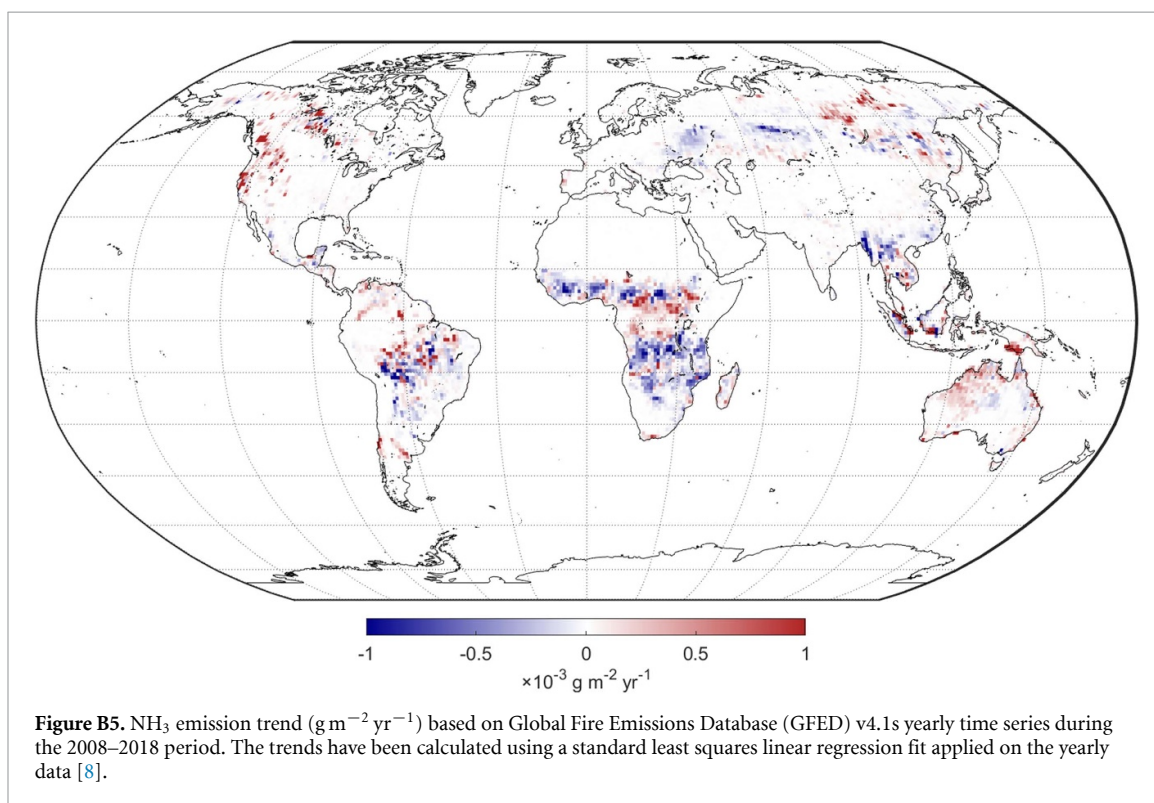
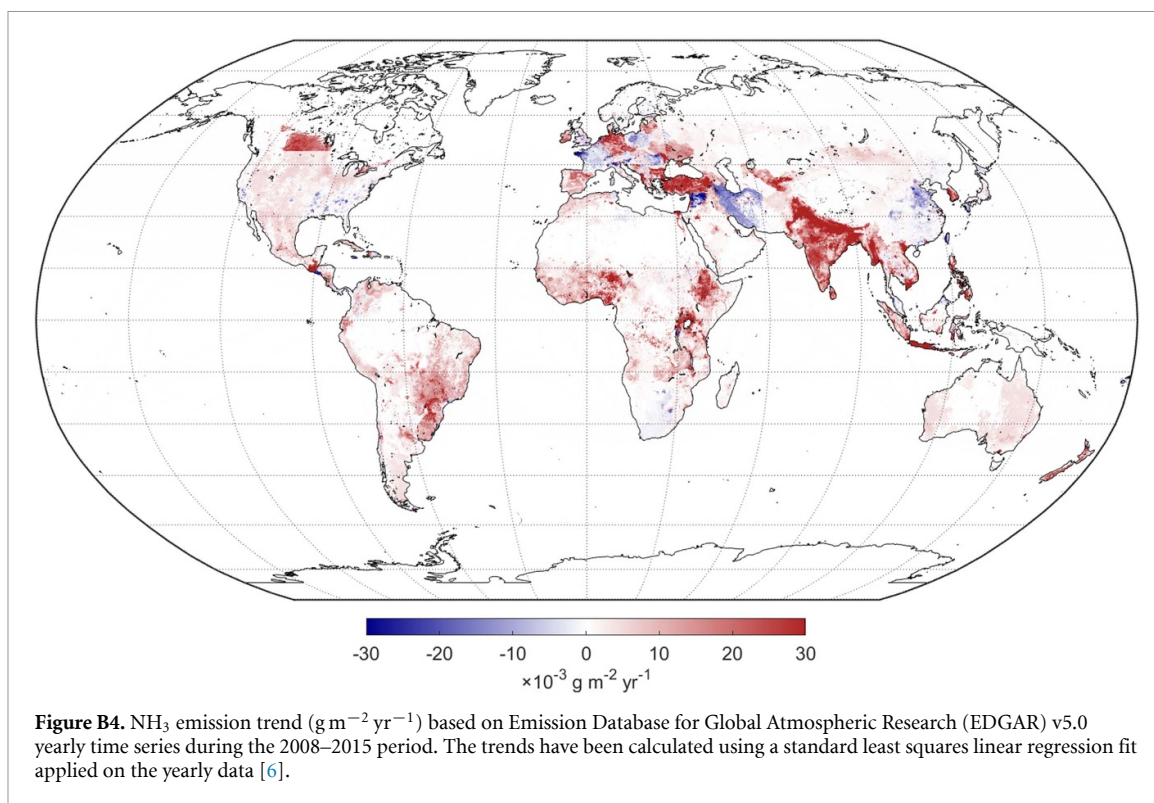


Table B1. National absolute ($\text{molec cm}^{-2} \text{ yr}^{-1}$), relative ($\% \text{ yr}^{-1}$) and decadal NH_3 trends ($\% \text{ 10yr}^{-1}$) based on national daily time series (2008–2018) measured by IASI/Metop-A. The relative trend is expressed as compound grow rate from 2008. Countries for which the calculated trend is significant are in bold.

	Absolute ($\text{molec cm}^{-2} \text{ yr}^{-1}$)	Relative ($\% \text{ yr}^{-1}$)	Decadal ($\% \text{ 10yr}^{-1}$)
Afghanistan	$(-1.3 \pm 2.5) \times 10^{13}$	-0.46 ± 0.85	-4.5 ± 8.8
Albania	$(-2.5 \pm 5.5) \times 10^{13}$	-1.2 ± 2.4	-12 ± 26
Algeria	$(0.2 \pm 1.9) \times 10^{13}$	0.07 ± 0.84	0.7 ± 8.7
Angola	$(9.4 \pm 2.3) \times 10^{13}$	2.57 ± 0.69	28.9 ± 7.1
Antarctica	$(21.7 \pm 3.2) \times 10^{12}$	1.03 ± 0.16	10.8 ± 1.6
Argentina	$(-13.7 \pm 2.7) \times 10^{13}$	-3.50 ± 0.58	-30.0 ± 6.0
Armenia	$(-5.6 \pm 3.7) \times 10^{13}$	-1.8 ± 1.1	-17 ± 11
Australia	$(-31.6 \pm 3.9) \times 10^{12}$	-4.53 ± 0.45	-37.1 ± 4.6
Austria	$(3.0 \pm 5.2) \times 10^{13}$	1.0 ± 1.7	10 ± 18
Azerbaijan	$(-11.0 \pm 4.7) \times 10^{13}$	-1.74 ± 0.67	-16.1 ± 6.9
Bahamas	$(-5.5 \pm 5.6) \times 10^{13}$	-14.3 ± 6.0	-79 ± 80
Bangladesh	$(-4.9 \pm 2.0) \times 10^{14}$	-2.24 ± 0.80	-20.3 ± 8.3
Belarus	$(3.1 \pm 8.7) \times 10^{13}$	0.9 ± 2.3	9 ± 25
Belgium	$(21.0 \pm 9.9) \times 10^{13}$	4.2 ± 2.2	50 ± 24
Belize	$(-9.0 \pm 8.5) \times 10^{13}$	-4.2 ± 2.9	-35 ± 33
Benin	$(5.9 \pm 1.2) \times 10^{14}$	3.64 ± 0.85	43.0 ± 8.8
Bhutan	$(-1.8 \pm 8.0) \times 10^{13}$	-0.6 ± 2.3	-6 ± 26
Bolivia	$(-18.1 \pm 6.7) \times 10^{13}$	-3.4 ± 1.0	-29 ± 11
Bosnia and Herz.	$(-1.8 \pm 5.5) \times 10^{13}$	-0.9 ± 2.2	-8 ± 25
Botswana	$(0.6 \pm 2.1) \times 10^{13}$	0.28 ± 0.90	2.8 ± 9.4
Brazil	$(12.1 \pm 3.1) \times 10^{13}$	1.94 ± 0.53	21.2 ± 5.4
Bulgaria	$(0.9 \pm 4.2) \times 10^{13}$	0.4 ± 1.8	4 ± 20
Burkina Faso	$(34.6 \pm 8.4) \times 10^{13}$	3.16 ± 0.85	36.5 ± 8.8
Burundi	$(23.4 \pm 6.4) \times 10^{13}$	2.86 ± 0.85	32.6 ± 8.9
Cabo Verde	$(-0.7 \pm 7.8) \times 10^{13}$	-0.2 ± 2.0	-2 ± 22
Cambodia	$(17.3 \pm 4.8) \times 10^{13}$	4.2 ± 1.3	51 ± 14
Cameroon	$(36.3 \pm 7.8) \times 10^{13}$	3.54 ± 0.87	41.6 ± 9.0
Canada	$(2.9 \pm 1.5) \times 10^{13}$	1.53 ± 0.83	16.4 ± 8.6
Central African Rep.	$(4.7 \pm 6.4) \times 10^{13}$	0.47 ± 0.64	4.8 ± 6.5
Chad	$(10.4 \pm 4.1) \times 10^{13}$	2.08 ± 0.86	22.8 ± 9.0
Chile	$(-60.7 \pm 8.4) \times 10^{12}$	-11.35 ± 0.93	-70.0 ± 9.7
People's Republic of China	$(24.7 \pm 2.1) \times 10^{13}$	6.25 ± 0.68	83.3 ± 7.0
Colombia	$(10.7 \pm 4.0) \times 10^{13}$	2.8 ± 1.1	32 ± 12
Congo	$(2.9 \pm 1.0) \times 10^{14}$	3.8 ± 1.4	45 ± 15
Costa Rica	$(2.8 \pm 4.5) \times 10^{13}$	2.6 ± 4.0	30 ± 47
Cote d'Ivoire	$(42.5 \pm 9.2) \times 10^{13}$	2.83 ± 0.68	32.2 ± 7.0
Croatia	$(4.5 \pm 5.5) \times 10^{13}$	1.4 ± 1.7	15 ± 18
Cuba	$(-5.2 \pm 2.0) \times 10^{13}$	-4.8 ± 1.4	-39 ± 15
Cyprus	$(12.2 \pm 5.7) \times 10^{13}$	3.6 ± 1.9	43 ± 20
Czechia	$(3.7 \pm 6.2) \times 10^{13}$	1.1 ± 1.8	12 ± 20
Dem. Rep. Congo	$(29.4 \pm 5.8) \times 10^{13}$	3.16 ± 0.70	36.5 ± 7.3
Denmark	$(11.5 \pm 7.7) \times 10^{13}$	3.9 ± 2.7	46 ± 31
Djibouti	$(0.2 \pm 4.0) \times 10^{13}$	0.1 ± 1.6	1 ± 17
Dominican Rep.	$(0.9 \pm 2.8) \times 10^{13}$	0.8 ± 2.3	8 ± 25
Ecuador	$(9.4 \pm 3.7) \times 10^{13}$	3.9 ± 1.7	47 ± 18
Egypt	$(5.8 \pm 1.9) \times 10^{13}$	2.39 ± 0.82	26.6 ± 8.6
El Salvador	$(3.7 \pm 4.5) \times 10^{13}$	1.5 ± 1.8	16 ± 19
Eritrea	$(0.7 \pm 2.9) \times 10^{13}$	0.3 ± 1.1	3 ± 11
Estonia	$(-3.0 \pm 7.7) \times 10^{13}$	-1.9 ± 3.8	-18 ± 45
Eswatini	$(-5.8 \pm 4.9) \times 10^{13}$	-3.3 ± 2.2	-29 ± 25
Ethiopia	$(1.8 \pm 2.0) \times 10^{13}$	0.34 ± 0.38	3.5 ± 3.9
Fiji	$(-3.1 \pm 6.1) \times 10^{13}$	-2.9 ± 4.2	-25 ± 51
Finland	$(-5.8 \pm 4.1) \times 10^{13}$	-4.5 ± 2.3	-37 ± 26
France	$(7.4 \pm 3.4) \times 10^{13}$	2.1 ± 1.0	24 ± 11
Gabon	$(29.3 \pm 9.7) \times 10^{13}$	4.6 ± 1.7	56 ± 19
Gambia	$(1.1 \pm 1.3) \times 10^{14}$	1.0 ± 1.1	10 ± 12
Georgia	$(-0.9 \pm 4.4) \times 10^{13}$	-0.3 ± 1.3	-3 ± 14
Germany	$(8.9 \pm 5.1) \times 10^{13}$	2.1 ± 1.2	23 ± 13
Ghana	$(5.6 \pm 1.2) \times 10^{14}$	3.28 ± 0.77	38.1 ± 8.0

Table B1. (Continued.)

	Absolute (molec cm ⁻² yr ⁻¹)	Relative (% yr ⁻¹)	Decadal (% 10yr ⁻¹)
Greece	$(-2.6 \pm 3.0) \times 10^{13}$	-1.5 ± 1.5	-14 ± 16
Greenland	$(-23.0 \pm 7.3) \times 10^{12}$	-1.11 ± 0.33	-10.5 ± 3.3
Guatemala	$(-7.9 \pm 4.5) \times 10^{13}$	-2.8 ± 1.3	-25 ± 14
Guinea	$(23.8 \pm 7.5) \times 10^{13}$	1.96 ± 0.65	21.4 ± 6.7
Guinea-Bissau	$(-0.1 \pm 1.5) \times 10^{14}$	-0.1 ± 1.1	-1 ± 12
Guyana	$(-0.8 \pm 4.4) \times 10^{13}$	-0.4 ± 2.1	-4 ± 23
Haiti	$(1.5 \pm 3.3) \times 10^{13}$	0.9 ± 1.9	9 ± 21
Honduras	$(-5.5 \pm 4.0) \times 10^{13}$	-3.3 ± 1.9	-28 ± 20
Hungary	$(7.5 \pm 5.4) \times 10^{13}$	2.0 ± 1.5	22 ± 16
Iceland	$(-6.4 \pm 4.1) \times 10^{13}$	-6.2 ± 2.7	-47 ± 30
India	$(0.8 \pm 1.0) \times 10^{14}$	0.39 ± 0.49	4.0 ± 5.0
Indonesia	$(10.1 \pm 5.1) \times 10^{13}$	2.7 ± 1.4	30 ± 15
Iran	$(-4.1 \pm 1.2) \times 10^{13}$	-3.71 ± 0.89	-31.5 ± 9.3
Iraq	$(4.5 \pm 3.7) \times 10^{13}$	2.5 ± 2.1	28 ± 23
Ireland	$(0.6 \pm 5.5) \times 10^{13}$	0.4 ± 3.2	4 ± 37
Israel	$(17.4 \pm 4.9) \times 10^{13}$	4.6 ± 1.5	56 ± 16
Italy	$(9.5 \pm 3.2) \times 10^{13}$	2.26 ± 0.82	25.0 ± 8.5
Jamaica	$(-1.8 \pm 5.6) \times 10^{13}$	-1.6 ± 3.8	-15 ± 45
Japan	$(8.3 \pm 2.9) \times 10^{13}$	7.7 ± 3.3	110 ± 38
Jordan	$(8.0 \pm 3.1) \times 10^{13}$	4.1 ± 1.8	50 ± 19
Kazakhstan	$(-4.1 \pm 1.9) \times 10^{13}$	-1.76 ± 0.71	-16.2 ± 7.3
Kenya	$(5.4 \pm 2.4) \times 10^{13}$	1.14 ± 0.52	12.0 ± 5.3
Kosovo	$(-1.3 \pm 6.3) \times 10^{13}$	-0.6 ± 2.7	-6 ± 30
Kuwait	$(6.7 \pm 7.2) \times 10^{13}$	5.9 ± 6.2	77 ± 83
Kyrgyzstan	$(-4.8 \pm 3.9) \times 10^{13}$	-0.97 ± 0.74	-9.3 ± 7.6
Laos	$(2.1 \pm 5.4) \times 10^{13}$	0.5 ± 1.2	5 ± 13
Latvia	$(-1.5 \pm 7.9) \times 10^{13}$	-0.7 ± 3.2	-7 ± 36
Lebanon	$(7.6 \pm 4.7) \times 10^{13}$	3.7 ± 2.5	44 ± 28
Lesotho	$(-0.7 \pm 2.4) \times 10^{13}$	-1.4 ± 3.6	-13 ± 42
Liberia	$(4.2 \pm 1.6) \times 10^{14}$	2.7 ± 1.1	30 ± 12
Libya	$(-1.0 \pm 1.4) \times 10^{13}$	-0.71 ± 0.97	-7 ± 10
Lithuania	$(4.5 \pm 8.3) \times 10^{13}$	1.5 ± 2.7	17 ± 30
Macedonia	$(-5.5 \pm 4.6) \times 10^{13}$	-4.0 ± 2.5	-33 ± 28
Madagascar	$(-1.0 \pm 1.4) \times 10^{13}$	-0.65 ± 0.81	-6.3 ± 8.4
Malawi	$(5.2 \pm 3.1) \times 10^{13}$	1.42 ± 0.88	15.2 ± 9.1
Malaysia	$(1.7 \pm 6.1) \times 10^{13}$	0.6 ± 1.9	6 ± 21
Mali	$(6.7 \pm 4.5) \times 10^{13}$	1.28 ± 0.87	13.6 ± 9.0
Mauritania	$(-0.8 \pm 3.9) \times 10^{13}$	-0.2 ± 1.2	-2 ± 12
Mexico	$(2.5 \pm 1.5) \times 10^{13}$	0.81 ± 0.51	8.4 ± 5.2
Moldova	$(4.1 \pm 5.5) \times 10^{13}$	1.2 ± 1.6	13 ± 17
Mongolia	$(-4.9 \pm 1.6) \times 10^{13}$	-3.22 ± 0.86	-27.9 ± 9.0
Montenegro	$(-6.7 \pm 8.5) \times 10^{13}$	-3.9 ± 3.5	-32 ± 41
Morocco	$(1.3 \pm 2.0) \times 10^{13}$	0.52 ± 0.80	5.3 ± 8.3
Mozambique	$(0.6 \pm 2.4) \times 10^{13}$	0.20 ± 0.83	2.1 ± 8.7
Myanmar	$(-18.9 \pm 5.0) \times 10^{13}$	-3.19 ± 0.70	-27.7 ± 7.3
N. Cyprus	$(20.2 \pm 5.8) \times 10^{13}$	5.7 ± 1.9	74 ± 21
Namibia	$(-0.2 \pm 1.6) \times 10^{13}$	-0.10 ± 0.85	-0.9 ± 8.8
Nepal	$(-1.4 \pm 1.1) \times 10^{14}$	-1.27 ± 0.89	-12.0 ± 9.2
Netherlands	$(2.1 \pm 1.1) \times 10^{14}$	3.6 ± 1.9	42 ± 21
New Caledonia	$(-5.8 \pm 5.2) \times 10^{13}$	-13.8 ± 5.4	-77 ± 70
New Zealand	$(-6.5 \pm 2.4) \times 10^{13}$	-4.7 ± 1.4	-38 ± 14
Nicaragua	$(-0.3 \pm 4.2) \times 10^{13}$	-0.2 ± 2.5	-2 ± 28
Niger	$(10.1 \pm 4.4) \times 10^{13}$	2.4 ± 1.1	26 ± 11
Nigeria	$(49.4 \pm 7.9) \times 10^{13}$	3.38 ± 0.62	39.4 ± 6.3
North Korea	$(33.8 \pm 6.5) \times 10^{13}$	14.7 ± 4.6	295 ± 57
Norway	$(-0.3 \pm 2.0) \times 10^{13}$	-0.2 ± 1.2	-2 ± 13
Oman	$(-5.9 \pm 4.0) \times 10^{13}$	-7.3 ± 3.1	-53 ± 36

(Continued)

Table B1. (Continued.)

	Absolute (molec cm ⁻² yr ⁻¹)	Relative (% yr ⁻¹)	Decadal (% 10yr ⁻¹)
Pakistan	$(3.8 \pm 1.5) \times 10^{14}$	1.86 ± 0.78	20.2 ± 8.1
Palestine	$(25.0 \pm 7.0) \times 10^{13}$	4.8 ± 1.6	60 ± 17
Panama	$(10.0 \pm 6.0) \times 10^{13}$	5.2 ± 3.4	67 ± 40
Papua New Guinea	$(1.0 \pm 3.7) \times 10^{13}$	0.6 ± 2.2	6 ± 24
Paraguay	$(-2.8 \pm 1.3) \times 10^{14}$	-2.8 ± 1.1	-25 ± 12
Peru	$(7.3 \pm 2.1) \times 10^{13}$	2.44 ± 0.75	27.2 ± 7.8
Philippines	$(2.7 \pm 3.2) \times 10^{13}$	1.2 ± 1.4	13 ± 15
Poland	$(8.6 \pm 4.9) \times 10^{13}$	2.4 ± 1.4	27 ± 15
Portugal	$(5.4 \pm 4.8) \times 10^{13}$	2.1 ± 1.9	23 ± 21
Puerto Rico	$(0.7 \pm 5.7) \times 10^{13}$	0.7 ± 5.2	8 ± 66
Romania	$(0.4 \pm 4.2) \times 10^{13}$	0.1 ± 1.3	1 ± 13
Russia	$(-7.1 \pm 1.7) \times 10^{13}$	-4.11 ± 0.80	-34.2 ± 8.3
Rwanda	$(32.4 \pm 6.0) \times 10^{13}$	4.04 ± 0.86	48.6 ± 9.0
S. Sudan	$(-8.4 \pm 5.5) \times 10^{13}$	-0.77 ± 0.47	-7.4 ± 4.8
Saudi Arabia	$(0.2 \pm 1.8) \times 10^{13}$	0.5 ± 3.3	5 ± 39
Senegal	$(9.5 \pm 8.7) \times 10^{13}$	0.95 ± 0.87	9.9 ± 9.1
Serbia	$(1.6 \pm 5.1) \times 10^{13}$	0.5 ± 1.5	5 ± 16
Sierra Leone	$(2.3 \pm 1.5) \times 10^{14}$	1.40 ± 0.92	14.9 ± 9.6
Slovakia	$(6.2 \pm 5.9) \times 10^{13}$	2.1 ± 2.0	23 ± 22
Slovenia	$(7.9 \pm 7.9) \times 10^{13}$	2.4 ± 2.4	27 ± 27
Solomon Is.	$(0.1 \pm 9.9) \times 10^{13}$	0.1 ± 6.2	1 ± 83
Somalia	$(-4.6 \pm 1.8) \times 10^{13}$	-2.26 ± 0.78	-20.4 ± 8.1
Somaliland	$(-5.2 \pm 2.4) \times 10^{13}$	-2.38 ± 0.93	-21.4 ± 9.7
South Africa	$(-7.3 \pm 8.0) \times 10^{12}$	-0.70 ± 0.72	-6.8 ± 7.5
South Korea	$(48.1 \pm 7.0) \times 10^{13}$	14.6 ± 3.6	291 ± 42
Spain	$(7.6 \pm 2.8) \times 10^{13}$	2.08 ± 0.82	22.9 ± 8.5
Sri Lanka	$(-12.8 \pm 5.2) \times 10^{13}$	-4.6 ± 1.4	-37 ± 15
Sudan	$(6.9 \pm 3.2) \times 10^{13}$	2.2 ± 1.1	25 ± 11
Suriname	$(1.2 \pm 5.1) \times 10^{13}$	0.5 ± 2.1	6 ± 23
Sweden	$(-0.0 \pm 2.7) \times 10^{13}$	-0.0 ± 1.6	-0 ± 18
Switzerland	$(4.9 \pm 5.5) \times 10^{13}$	1.7 ± 1.8	18 ± 20
Syria	$(3.9 \pm 3.2) \times 10^{13}$	1.6 ± 1.3	17 ± 14
Taiwan	$(20.8 \pm 7.0) \times 10^{13}$	4.0 ± 1.5	49 ± 16
Tajikistan	$(-12.9 \pm 4.0) \times 10^{13}$	-2.74 ± 0.73	-24.3 ± 7.6
Tanzania	$(11.2 \pm 3.1) \times 10^{13}$	1.98 ± 0.59	21.7 ± 6.1
Thailand	$(12.3 \pm 4.5) \times 10^{13}$	2.15 ± 0.84	23.8 ± 8.7
Timor-Leste	$(-1.3 \pm 5.1) \times 10^{13}$	-1.0 ± 3.3	-10 ± 38
Togo	$(5.9 \pm 1.3) \times 10^{14}$	3.41 ± 0.87	39.9 ± 9.1
Tunisia	$(7.6 \pm 3.8) \times 10^{13}$	1.74 ± 0.90	18.8 ± 9.4
Turkey	$(6.0 \pm 1.4) \times 10^{13}$	3.31 ± 0.89	38.5 ± 9.3
Turkmenistan	$(-11.0 \pm 3.7) \times 10^{13}$	-2.55 ± 0.74	-22.8 ± 7.6
Uganda	$(21.2 \pm 4.5) \times 10^{13}$	2.18 ± 0.50	24.0 ± 5.1
Ukraine	$(-3.6 \pm 4.2) \times 10^{13}$	-1.2 ± 1.2	-11 ± 13
United Arab Emirates	$(-4.9 \pm 4.6) \times 10^{13}$	-6.5 ± 3.9	-49 ± 46
United Kingdom	$(6.1 \pm 4.5) \times 10^{13}$	2.9 ± 2.2	33 ± 24
United States of America	$(11.4 \pm 1.7) \times 10^{13}$	3.42 ± 0.59	39.9 ± 6.1
Uruguay	$(-8.0 \pm 7.3) \times 10^{13}$	-1.7 ± 1.4	-16 ± 14
Uzbekistan	$(-5.4 \pm 6.0) \times 10^{13}$	-0.96 ± 0.98	-9 ± 10
Vanuatu	$(6.9 \pm 9.5) \times 10^{13}$	13 ± 15	$(2.3 \pm 3.1) \times 10^2$
Venezuela, Bolivarian Republic of	$(1.2 \pm 2.6) \times 10^{13}$	0.42 ± 0.86	4.3 ± 9.0
Vietnam	$(17.9 \pm 4.3) \times 10^{13}$	4.4 ± 1.2	54 ± 13
W. Sahara	$(0.5 \pm 3.7) \times 10^{13}$	0.5 ± 3.5	6 ± 41
Yemen	$(-2.0 \pm 2.1) \times 10^{13}$	-2.8 ± 2.3	-25 ± 26
Zambia	$(7.9 \pm 2.2) \times 10^{13}$	2.20 ± 0.66	24.3 ± 6.8
Zimbabwe	$(1.4 \pm 2.7) \times 10^{13}$	0.51 ± 0.99	5 ± 10

ORCID iDs

Martin Van Damme  <https://orcid.org/0000-0003-1752-0558>

Lieven Clarisse  <https://orcid.org/0000-0002-8805-2141>

Bruno Franco  <https://orcid.org/0000-0003-0736-458X>

Mark A Sutton  <https://orcid.org/0000-0002-1342-2072>

Jan Willem Erisman  <https://orcid.org/0000-0001-5058-7012>

Roy Wichink Kruit  <https://orcid.org/0000-0003-4956-650X>

Margreet van Zanten  <https://orcid.org/0000-0003-0010-7839>

Simon Whitburn  <https://orcid.org/0000-0003-3279-8152>

Cathy Clerbaux  <https://orcid.org/0000-0003-0394-7200>

Pierre-François Coheur  <https://orcid.org/0000-0002-5022-8842>

References

- [1] Sutton M A *et al* 2013 Towards a climate-dependent paradigm of ammonia emission and deposition *Philos. Trans. R. Soc. B* **368** 20130166
- [2] European Environment Agency (EEA) 2020 European Union emission inventory report 1990–2018 under the UNECE Convention on Long-Range Transboundary Air Pollution (LRTAP) *EEA Report 05/2020*
- [3] Bray C D *et al* 2018 Ammonia emissions from biomass burning in the continental United States *Atmos. Environ.* **187** 50–61
- [4] Zhang X *et al* 2017 Ammonia emissions may be substantially underestimated in China *Environ. Sci. Technol.* **51** 12089–96
- [5] Crippa M *et al* 2018 Gridded emissions of air pollutants for the period 1970–2012 within EDGAR v4.3.2 *Earth Syst. Sci. Data* **10** 1987–2013
- [6] Emissions Database for Global Atmospheric Research (EDGAR) 2020 v5.0 Global Air Pollutant Emissions (available at: https://edgar.jrc.ec.europa.eu/overview.php?v=50_AP) (Accessed 3 November 2020)
- [7] Behera S, Sharma M, Aneja V and Balasubramanian R 2013 Ammonia in the atmosphere: a review on emission sources, atmospheric chemistry and deposition on terrestrial bodies *Environ. Sci. Pollut. Res. Int.* **20** 8092–131
- [8] Global Fire Emissions Database version 4.1 including small fire burned area (GFED4s) 2020 (available at: www.geo.vu.nl/gwerf/GFED/GFED4/) (Accessed 22 October)
- [9] Van Damme M *et al* 2018 Industrial and agricultural ammonia point sources exposed *Nature* **564** 99–103
- [10] Diaz R J and Rosenberg R 2008 Spreading dead zones and consequences for marine ecosystems *Science* **321** 926–9
- [11] Dise N B *et al* 2011 Nitrogen as a threat to European terrestrial biodiversity *The European Nitrogen Assessment: Sources, Effects and Policy Perspectives* (Cambridge: Cambridge University Press) (<http://doi.org/10.1017/CBO9780511976988.023>)
- [12] Dammers E *et al* 2019 NH₃ emissions from large point sources derived from CrIS and IASI satellite observations *Atmos. Chem. Phys.* **19** 12261–93
- [13] Bobbink R *et al* 2010 Global assessment of nitrogen deposition effects on terrestrial plant diversity: a synthesis *Ecol. Appl.* **20**:1 30–59
- [14] Ellis R A *et al* 2013 Present and future nitrogen deposition to national parks in the United States: critical load exceedances *Atmos. Chem. Phys.* **13** 9083–95
- [15] Pope C A, Ezzati M III and Dockery D W 2009 Fine-particulate air pollution and life expectancy in the United States *N. Engl. J. Med.* **360** 376–86
- [16] Lelieveld J, Evans J S, Fnais M, Giannadaki D and Pozzer A 2015 The contribution of outdoor air pollution sources to premature mortality on a global scale *Nature* **525** 367–71
- [17] Erisman J W and Schaap M 2004 The need for ammonia abatement with respect to secondary PM reductions in Europe *Environ. Pollut.* **129** 159–63
- [18] Wang S *et al* 2015 Atmospheric ammonia and its impacts on regional air quality over the megacity of Shanghai, China *Sci. Rep.* **5** 15842
- [19] Wu Y *et al* 2016 PM_{2.5} pollution is substantially affected by ammonia emissions in China *Environ. Pollut.* **218** 86–94
- [20] Sutton M A *et al* 2020 Alkaline air: changing perspectives on nitrogen and air pollution in an ammonia-rich world *Philos. Trans. R. Soc. A* **378** 20190315
- [21] Saylor R, Myles L, Sibble D, Caldwell J and Xing J 2014 Recent trends in gas-phase ammonia and PM_{2.5} ammonium in the Southeast United States *J. Air Waste Manage. Assoc.* **65** 347–57
- [22] van Zanten M, Wichink Kruit R, Hoogerbrugge R, Van der Swaluw E and van Pul W 2017 Trends in ammonia measurements in The Netherlands over the period 1993–2014 *Atmos. Environ.* **148** 352–60
- [23] Tang Y S *et al* 2018 Drivers for spatial, temporal and long-term trends in atmospheric ammonia and ammonium in the UK *Atmos. Chem. Phys.* **18** 705–33
- [24] Lachatre M *et al* 2019 The unintended consequence of SO₂ and NO₂ regulations over China: increase of ammonia levels and impact on PM_{2.5} concentrations *Atmos. Chem. Phys.* **19** 6701–16
- [25] Paulot F and Jacob D J 2014 Hidden cost of U.S. agricultural exports: particulate matter from ammonia emissions *Environ. Sci. Technol.* **48** 903–8
- [26] Backes A M, Aulinger A, Bieser J, Matthias V and Quante M 2016 Ammonia emissions in Europe, part II: how ammonia emission abatement strategies affect secondary aerosols *Atmos. Environ.* **126** 153–61
- [27] Liu M *et al* 2019 Ammonia emission control in China would mitigate haze pollution and nitrogen deposition, but worsen acid rain *Proc. Natl Acad. Sci.* **116** 7760–5
- [28] Shindell D T *et al* 2009 Improved attribution of climate forcing to emissions *Science* **326** 716–18
- [29] Butterbach-Bahl K *et al* 2011 Nitrogen as a threat to the European greenhouse balance *The European Nitrogen Assessment: Sources, Effects and Policy Perspectives* (Cambridge: Cambridge University Press) (<https://doi.org/10.1017/CBO9780511976988.022>)
- [30] Reis S, Pinder R W, Zhang M, Lijie G and Sutton M A 2009 Reactive nitrogen in atmospheric emission inventories *Atmos. Chem. Phys.* **9** 7657–77
- [31] Official Journal of the European Union 2016 Directive (EU) 2016/2284 of the European Parliament and of the Council of 14 December 2016 on the reduction of national emissions of certain atmospheric pollutants, amending Directive 2003/35/EC and repealing Directive 2001/81/EC (available at: <http://data.europa.eu/eli/dir/2016/2284/oj>) (Accessed 13 November 2020)
- [32] Clarisse L, Clerbaux C, Dentener F, Hurtmans D and Coheur P-F 2009 Global ammonia distribution derived from infrared satellite observations *Nat. Geosci.* **2** 479–83
- [33] Shephard M W and Cady-Pereira K E 2015 Cross-track Infrared Sounder (CrIS) satellite observations of tropospheric ammonia *Atmos. Meas. Tech.* **8** 1323–36
- [34] Warner J X, Wei Z, Strow L L, Dickerson R R and Nowak J B 2016 The global tropospheric ammonia distribution as seen in the 13-year AIRS measurement record *Atmos. Chem. Phys.* **16** 5467–79

- [35] Someya Y, Imasu R, Shiomi K and Saitoh N 2020 Atmospheric ammonia retrieval from the TANSO-FTS/GOSAT thermal infrared sounder *Atmos. Meas. Tech.* **13** 309–21
- [36] Clarisse L, Van Damme M, Clerbaux C and Coheur P-F 2019 Tracking down global NH₃ point sources with wind-adjusted superresolution *Atmos. Meas. Tech.* **12** 5457–73
- [37] Warner J X et al 2017 Increased atmospheric ammonia over the world's major agricultural areas detected from space *Geophys. Res. Lett.* **44** 2875–84
- [38] Liu L et al 2019 Estimating global surface ammonia concentrations inferred from satellite retrievals *Atmos. Chem. Phys.* **19** 12051–66
- [39] Kharol S K et al 2018 Dry deposition of reactive nitrogen from satellite observations of ammonia and nitrogen dioxide over North America *Geophys. Res. Lett.* **45** 1157–66
- [40] Liu L et al 2020 Global estimates of dry ammonia deposition inferred from space-measurements *Sci. Total Environ.* **730** 139189
- [41] Shephard M W et al 2020 Ammonia measurements from space with the Cross-track Infrared Sounder: characteristics and applications *Atmos. Chem. Phys.* **20** 2277–302
- [42] Chen Y et al 2020 High-resolution hybrid inversion of IASI ammonia columns to constrain U.S. ammonia emissions using the CMAQ adjoint model *Atmos. Chem. Phys. Discuss.* **2020** 1–25
- [43] Cao H et al 2020 Inverse modeling of NH₃ sources using CrIS remote sensing measurements *Environ. Res. Lett.* **15** 104082
- [44] Stokstad E 2019 Nitrogen crisis threatens Dutch environment and economy *Science* **366** 1180–1
- [45] Clerbaux C et al 2009 Monitoring of atmospheric composition using the thermal infrared IASI/MetOp sounder *Atmos. Chem. Phys.* **9** 6041–54
- [46] Clarisse L et al 2010 Satellite monitoring of ammonia: a case study of the San Joaquin Valley *J. Geophys. Res.* **115** D13302
- [47] Van Damme M et al 2014 Global distributions, time series and error characterization of atmospheric ammonia (NH₃) from IASI satellite observations *Atmos. Chem. Phys.* **14** 2905–22
- [48] Van Damme M et al 2014 Evaluating 4 years of atmospheric ammonia (NH₃) over Europe using IASI satellite observations and LOTOS-EUROS model results *J. Geophys. Res. Atmos.* **119** 9549–66
- [49] Van Damme M et al 2015 Worldwide spatiotemporal atmospheric ammonia (NH₃) columns variability revealed by satellite *Geophys. Res. Lett.* **42** 8660–8
- [50] Whitburn S et al 2016 Doubling of annual ammonia emissions from the peat fires in Indonesia during the 2015 El Niño *Geophys. Res. Lett.* **43** 11007–14
- [51] Viatte C et al 2020 Atmospheric ammonia variability and link with particulate matter formation: a case study over the Paris area *Atmos. Chem. Phys.* **20** 577–96
- [52] Whitburn S et al 2016 A flexible and robust neural network IASI-NH₃ retrieval algorithm *J. Geophys. Res. Atmos.* **121** 6581–99
- [53] Van Damme M et al 2017 Version 2 of the IASI NH₃ neural network retrieval algorithm: near-real-time and reanalysed datasets *Atmos. Meas. Tech.* **10** 4905–14
- [54] Franco B et al 2018 A general framework for global retrievals of trace gases from IASI: application to methanol, formic acid and PAN *J. Geophys. Res. Atmos.* **123** 13963–84
- [55] Franco B et al 2019 Acetone atmospheric distribution retrieved from space *Geophys. Res. Lett.* **46** 2884–93
- [56] Franco B et al 2020 Spaceborne measurements of formic and acetic acids: a global view of the regional sources *Geophys. Res. Lett.* **47** e2019GL086239
- [57] August T et al 2012 IASI on Metop-A: operational level 2 retrievals after five years in orbit *J. Quant. Spectrosc. Radiat. Transfer.* **113** 1340–71
- [58] Hersbach H et al 2020 The ERA5 global reanalysis *Quart. J. R. Meteor. Soc.* **146** 1999–2049
- [59] Clarisse L et al 2019 A decadal data set of global atmospheric dust retrieved from IASI satellite measurements *J. Geophys. Res. Atmos.* **124** 1618–47
- [60] Van Damme M et al 2015 Towards validation of ammonia (NH₃) measurements from the IASI satellite *Atmos. Meas. Tech.* **8** 1575–91
- [61] Dammers E et al 2016 An evaluation of IASI-NH₃ with ground-based Fourier transform infrared spectroscopy measurements *Atmos. Chem. Phys.* **16** 10351–68
- [62] Guo X et al 2021 Validation of IASI satellite ammonia observations at the pixel scale using in-situ vertical profiles *J. Geophys. Res. Atmos.* **126** e2020JD033475
- [63] Gardiner T et al 2008 Trend analysis of greenhouse gases over Europe measured by a network of ground-based remote FTIR instruments *Atmos. Chem. Phys.* **8** 6719–27
- [64] Cox M G, Harris P M, Milton M J T and Woods P T 2002 Method for evaluating trends in ozone concentration data and its application to data from the UK rural ozone monitoring network *National Physical Laboratory (NPL) Report CMSC 15/02*
- [65] Fu H, Luo Z and Hu S 2020 A temporal-spatial analysis and future trends of ammonia emissions in China *Sci. Total Environ.* **731** 138897
- [66] Pan Y et al 2016 Fossil fuel combustion-related emissions dominate atmospheric ammonia sources during severe haze episodes: evidence from 15N-stable isotope in size-resolved aerosol ammonium *Environ. Sci. Technol.* **50** 8049–56
- [67] Liu J et al 2018 Evidence of rural and suburban sources of urban haze formation in China: a case study from the Pearl River Delta region *J. Geophys. Res. Atmos.* **123** 4712–26
- [68] Chang Y et al 2019 Assessing contributions of agricultural and nonagricultural emissions to atmospheric ammonia in a Chinese megacity *Environ. Sci. Technol.* **53** 1822–33
- [69] Zheng B et al 2018 Trends in China's anthropogenic emissions since 2010 as the consequence of clean air actions *Atmos. Chem. Phys.* **18** 14095–111
- [70] Liu M et al 2018 Rapid SO₂ emission reductions significantly increase tropospheric ammonia concentrations over the North China Plain *Atmos. Chem. Phys.* **18** 17933–43
- [71] Organisation for Economic Co-operation and Development (OECD) 2020 Agri-environmental Indicators (AEIs) database (available at: <https://stats.oecd.org/>) (Accessed 5 November 2020)
- [72] Lee S, Ho C-H, Lee Y G, Choi H-J and Song C-K 2013 Influence of transboundary air pollutants from China on the high-PM10 episode in Seoul, Korea for the period October 16–20, 2008 *Atmos. Environ.* **77** 430–9
- [73] Lee H-J, Jo H-Y, Kim S-W, Park M-S and Kim C-H 2019 Impacts of atmospheric vertical structures on transboundary aerosol transport from China to South Korea *Sci. Rep.* **9** 13040
- [74] Onishi K et al 2012 Atmospheric transport route determines components of Asian dust and health effects in Japan *Atmos. Environ.* **49** 94–102
- [75] Raza S et al 2018 Piling up reactive nitrogen and declining nitrogen use efficiency in Pakistan: a challenge not challenged (1961–2013) *Environ. Res. Lett.* **13** 034012
- [76] Shahzad A N, Qureshi M K, Wakeel A and Misselbrook T 2019 Crop production in Pakistan and low nitrogen use efficiencies *Nat. Sustain.* **2** 1106–14
- [77] Xu R T et al 2018 Half-century ammonia emissions from agricultural systems in Southern Asia: magnitude, spatiotemporal patterns and implications for human health *GeoHealth* **2** 40–53
- [78] Kuttippurath J et al 2020 Record high levels of atmospheric ammonia over India: spatial and temporal analyses *Sci. Total Environ.* **740** 139986

- [79] Sutton M *et al* 2017 The Indian Nitrogen Challenge in a Global Perspective *The Indian Nitrogen Assessment* (Amsterdam: Elsevier)
- [80] Kim D-G, Saggarr S and Roudier P 2012 The effect of nitrification inhibitors on soil ammonia emissions in nitrogen managed soils: a meta-analysis *Nutr. Cycling Agroecosyst.* **93** 51–64
- [81] Singh B 2019 Neem coated urea as a source of nitrogen for plants *J. Eco-friendly Agric.* **14** 43–54
- [82] IGBP-DIS 1998 SoilData(V.0) A program for creating global soil-property databases IGBP Global Soils Data Task, France (available at: https://nelson.wisc.edu/sage/data-and-models/atlas/maps/soilph/atl_soilph_asi.jpg) (Accessed 14 November 2020)
- [83] Yulsman T 2018 Smoke from Siberian fires blows all the way to Canada—and is seen by a satellite nearly a million miles from Earth (available at: www.discovermagazine.com/environment/smoke-from-siberian-fires-blows-all-the-way-to-canada-and-is-seen-by-a-satellite-nearly-a-million-miles-from-earth) (Accessed 14 November 2020)
- [84] NASA 2018 Smoke from Siberian fires reaches Canada (available at: www.nasa.gov/image-feature/goddard/2018/smoke-from-siberian-fires-reaches-canada) (Accessed 14 November 2020)
- [85] R'Honi Y *et al* 2013 Exceptional emissions of NH₃ and HCOOH in the 2010 Russian wildfires *Atmos. Chem. Phys.* **13** 4171–81
- [86] Hari V, Rakovec O, Markonis Y, Hanel M and Kumar R 2020 Increased future occurrences of the exceptional 2018–2019 Central European drought under global warming *Sci. Rep.* **10** 12207
- [87] Hoogerbrugge R *et al* 2019 Grootschalige concentratie—en depositiekaarten Nederland (available at: <https://rivm.openrepository.com/handle/10029/623233>)
- [88] KNMI 2019 Jaar 2018—extreem warm, extreem zonnig en zeer droog (available at: <https://knmi.nl/nederland-nu/klimatologie/maand-en-seizoensoverzichten/2018/jaar>) (Accessed 9 December 2020)
- [89] European Environment Agency (EEA) 2020 Air pollutant emissions data viewer (Gothenburg Protocol, LRTAP Convention) 1990–2018 (available at: www.eea.europa.eu/data-and-maps/dashboards/air-pollutant-emissions-data-viewer-3) (Accessed 8 November 2020)
- [90] European Environment Agency (EEA) 2019 The European environment: state and outlook 2020 (available at: www.eea.europa.eu/publications/soer-2020)
- [91] Horvath L, Fagerli H and Sutton M A 2009 Long-term record (1981–2005) of ammonia and ammonium concentrations at K-Puszt Hungary and the effect of sulphur dioxide emission change on measured and modelled concentrations *Atmospheric Ammonia* (Dordrecht: Springer) 181–5
- [92] Yeni O and Teoman Ö 2020 The agriculture–environment relationship and environment-based agricultural support instruments in Turkey *Eur. Rev.* **1**–25
- [93] Food and Agriculture Organization of the United Nations (FAO) 2020 FAOSTAT fertilizers by nutrient dataset (available at: www.fao.org/faostat/en/#data/RFN) (Accessed 6 November 2020)
- [94] Elrys A S *et al* 2019 Budgeting nitrogen flows and the food nitrogen footprint of Egypt during the past half century: challenges and opportunities *Environ. Int.* **130** 104895
- [95] Whitburn S *et al* 2015 Ammonia emissions in tropical biomass burning regions: comparison between satellite-derived emissions and bottom-up fire inventories *Atmos. Environ.* **121** 42–54
- [96] Hickman J E *et al* Changes in biomass burning, wetland extent, or agriculture drive atmospheric NH₃ trends in several African regions *Atmos. Chem. Phys. Disc.* **2020** 1–33 in review
- [97] Food and Agriculture Organization (FAO) Crisis in South Sudan FAO in emergencies 2020 (available at: www.fao.org/emergencies/crisis/south-sudan/intro/en/) (Accessed 8 November 2020)
- [98] Idris I 2018 Livestock and conflict in South Sudan *K4D Helpdesk Report* 484 (Brighton: Institute of Development Studies) (available at: <https://gsdrc.org/publications/livestock-and-conflict-in-south-sudan/>) (Accessed 8 November 2020)
- [99] Jankowski K *et al* 2018 Deep soils modify environmental consequences of increased nitrogen fertilizer use in intensifying Amazon agriculture *Sci. Rep.* **8** 13478
- [100] Yu F, Nair A A and Luo G 2018 Long-term trend of gaseous ammonia over the United States: modeling and comparison with observations *J. Geophys. Res. Atmos.* **123** 8315–25
- [101] Schiferl L D *et al* 2016 Interannual variability of ammonia concentrations over the United States: sources and implications *Atmos. Chem. Phys.* **16** 12305–28
- [102] Yao X and Zhang L 2019 Causes of large increases in atmospheric ammonia in the last decade across North America *ACS Omega* **4** 22133–42
- [103] Environmental Protection Agency (EPA) 2020 Air pollutant emissions trends data (available at: www.epa.gov/sites/production/files/2018-04/national_tier1_caps.xlsx) (Accessed 6 November 2020)
- [104] Environmental Protection Agency (EPA) 2020 Air pollutant emissions trends data (available at: www.epa.gov/sites/production/files/2018-07/state_tier1_caps.xlsx) (Accessed 6 November 2020)
- [105] Li Y *et al* 2016 Increasing importance of deposition of reduced nitrogen in the United States *Proc. Natl Acad. Sci.* **113** 5874–9
- [106] Yamanouchi S *et al* 2021 Multiscale observations of NH₃ around Toronto, Canada *Atmos. Meas. Tech.* **14** 905–21
- [107] Canada 2020 Air pollutants emissions inventory (APEI) (available at: <https://pollution-waste.canada.ca/air-emission-inventory>) (Accessed 6 November 2020)
- [108] Adams C *et al* 2019 Satellite-derived emissions of carbon monoxide, ammonia and nitrogen dioxide from the 2016 Horse River wildfire in the Fort McMurray area *Atmos. Chem. Phys.* **19** 2577–99
- [109] Lutsch E *et al* 2019 Unprecedented atmospheric ammonia concentrations detected in the high Arctic from the 2017 Canadian wildfires *J. Geophys. Res. Atmos.* **124** 8178–202
- [110] Buijsman E, Aben J M, Van Elzakker B G and Mennen M G 1998 An automatic atmospheric ammonia network in The Netherlands set-up and results *Atmos. Environ.* **32** 317–24
- [111] Lolkema D E *et al* 2015 The measuring ammonia in nature (MAN) network in The Netherlands *Biogeosciences* **12** 5133–42
- [112] Noordijk H *et al* 2020 Performance of the MAN ammonia monitoring network in The Netherlands *Atmos. Environ.* **228** 117400
- [113] Erisman J W, Mosquera J and Hensen A 2001 Two options to explain the ammonia gap in The Netherlands *Environ. Sci. Policy* **4** 97–105
- [114] Erisman J W, Bleeker A and van Jaarsveld J 1998 Evaluation of ammonia emission abatement on the basis of measurements and model calculations *Environ. Pollut.* **102** 269–74
- [115] Erisman J W and Monteny G 1998 Consequences of new scientific findings for future abatement of ammonia emissions *Environ. Pollut.* **102** 275–82
- [116] Wichink Kruit R *et al* 2017 Modelling trends in ammonia in The Netherlands over the period 1990–2014 *Atmos. Environ.* **154** 20–30
- [117] Official Journal of the European Union 2019 Judgment of the Court (Second Chamber) of 7 November 2018 (requests for a preliminary ruling from the Raad van State—Netherlands) (2019/C 16/15) (available at: <https://eur-lex.europa.eu/legal-content/EN/TXT/PDF/?uri=CELEX:62017CA0293&from=DE>) (Accessed 10 October 2020)

- [118] Bittman S, Dedina M C M H, Oenema O and Sutton M 2014 *Options for Ammonia Mitigation: Guidance from the UNECE Task Force on Reactive Nitrogen* (Edinburgh: Centre for Ecology & Hydrology, on behalf of Task Force on Reactive Nitrogen of the UNECE Convention on Long Range Transboundary Air Pollution)
- [119] Reis S, Howard C and Sutton M A (eds) 2015 *Costs of Ammonia Abatement and the Climate Co-Benefits* (Dordrecht: Springer) (<http://doi.org/10.1007/978-94-017-9722-1>)
- [120] Giannakis E, Kushta J, Bruggeman A and Lelieveld J 2019 Costs and benefits of agricultural ammonia emission abatement options for compliance with European air quality regulations *Environ. Sci. Eur.* **31** 93
- [121] Zhang X *et al* 2020 Societal benefits of halving agricultural ammonia emissions in China far exceed the abatement costs *Nat. Commun.* **11** 4357
- [122] Sutton M A and Howard C M 2018 Satellite pinpoints ammonia sources globally *Nature* **564** 49–50
- [123] Kanter D R *et al* 2020 Nitrogen pollution policy beyond the farm *Nat. Food* **1** 27–32
- [124] United Nations Environment Programme (UNEP) 2019 Sustainable nitrogen management. Resolution adopted by the United Nations Environment Assembly (UNEP/EA.4/Res.14) on 15 March (available at: <https://papersmart.unon.org/resolution/uploads/k1900699.pdf>)
- [125] Taylor I A *et al* 2018 Exploring the utility of IASI for monitoring volcanic SO₂ emissions *J. Geophys. Res. Atmos.* **123** 5588–606
- [126] Bouillon M *et al* 2020 Ten-year assessment of IASI radiance and temperature *Remote Sens.* **12** 2393